

The Structural Basis of Rubisco Phase Separation in the Pyrenoid

Shan He¹, Hui-Ting Chou^{2,9}, Doreen Matthies², Tobias Wunder³, Moritz T. Meyer¹, Nicky Atkinson⁴, Antonio Martinez-Sanchez^{5,6}, Philip D. Jeffrey¹, Sarah A. Port¹, Weronika Patena¹, Guanhua He¹, Vivian K. Chen⁷, Frederick M. Hughson¹, Alistair J. McCormick⁴, Oliver Mueller-Cajar³, Benjamin D. Engel^{5,8}, Zhiheng Yu², Martin C. Jonikas^{1,*}

¹Department of Molecular Biology, Princeton University, Princeton, NJ 08544, USA. ²Janelia Research Campus, Howard Hughes Medical Institute, 19700 Helix Drive, Ashburn, VA 20147, USA. ³School of Biological Sciences, Nanyang Technological University, 60 Nanyang Drive, Singapore 637551, Singapore. ⁴SynthSys & Institute of Molecular Plant Sciences, School of Biological Sciences, University of Edinburgh, Edinburgh, EH9 3BF, UK. ⁵Department of Molecular Structural Biology, Max Planck Institute of Biochemistry, 82152 Martinsried, Germany. ⁶Institute of Neuropathology, University of Göttingen Medical Center, 37075 Göttingen, Germany. ⁷Department of Biology, Stanford University, Stanford, CA 94305, USA. ⁸Helmholtz Pioneer Campus, Helmholtz Zentrum München, 85764 Neuherberg, Germany. ⁹Present address: Department of Therapeutic Discovery, Amgen Discovery Research, Amgen Inc., South San Francisco, CA 94080, USA.

*Correspondence and Lead Contact: mjonikas@princeton.edu.

21 **Abstract**

22 Approximately one-third of global CO₂ fixation occurs in a phase-separated algal organelle called
23 the pyrenoid. Existing data suggest that the pyrenoid forms by the phase separation of the CO₂-
24 fixing enzyme Rubisco with a linker protein; however, the molecular interactions underlying this
25 phase separation remain unknown. Here we present the structural basis of the interactions between
26 Rubisco and its intrinsically disordered linker protein EPYC1 (Essential Pyrenoid Component 1)
27 in the model alga *Chlamydomonas reinhardtii*. We find that EPYC1 consists of five evenly-spaced
28 Rubisco-binding regions that share sequence similarity. Single-particle cryo-electron microscopy
29 of one of these regions in complex with Rubisco indicates that each Rubisco holoenzyme has eight
30 binding sites for EPYC1, one on each Rubisco small subunit. Interface mutations disrupt binding,
31 phase separation, and pyrenoid formation. Cryo-electron tomography supports a model where
32 EPYC1 and Rubisco form a co-dependent multivalent network of specific low-affinity bonds,
33 giving the matrix liquid-like properties. Our results advance the structural and functional
34 understanding of the phase separation underlying the pyrenoid, an organelle that plays a
35 fundamental role in the global carbon cycle.

36 Main Text

37 The CO₂-fixing enzyme Rubisco drives the global carbon cycle, mediating the assimilation
38 of approximately 100 gigatons of carbon per year¹. The gradual decrease of atmospheric CO₂ over
39 billions of years² has made Rubisco's job increasingly difficult, to the point where CO₂
40 assimilation limits the growth rate of many photosynthetic organisms³. This selective pressure is
41 thought to have led to the evolution of CO₂ concentrating mechanisms, which feed concentrated
42 CO₂ to Rubisco to enhance growth⁴. Of these mechanisms, the most poorly understood relies on
43 the pyrenoid, a phase separated organelle⁵ found in the chloroplast of nearly all eukaryotic algae
44 and some land plants (Fig. 1a, b)^{6,7}. The pyrenoid enhances the activity of Rubisco by clustering
45 it around modified thylakoid membranes that supply Rubisco with concentrated CO₂^{8,9}.

46 For decades, the mechanism for packaging the Rubisco holoenzyme into the pyrenoid
47 remained unknown. Recent work showed that in the leading model alga *Chlamydomonas*
48 *reinhardtii* (*Chlamydomonas* hereafter), the clustering of Rubisco into the pyrenoid matrix
49 requires the Rubisco-binding protein EPYC1¹⁰. EPYC1 and Rubisco are the most abundant
50 components of the pyrenoid and bind to each other. Moreover, combining purified EPYC1 and
51 Rubisco together produces phase-separated condensates¹¹ that mix internally at a rate similar to
52 that observed for the matrix *in vivo*⁵, suggesting that these two proteins are sufficient to form the
53 structure of the pyrenoid matrix. The sequence repeats within EPYC1 and eight-fold symmetry of
54 the Rubisco holoenzyme led us to hypothesize that EPYC1 and Rubisco each have multiple
55 binding sites for the other, allowing the two proteins to form a co-dependent condensate (Fig. 1c)¹⁰.

56 Here, we determined the structural basis that underlies the EPYC1-Rubisco condensate.
57 Using biophysical approaches, we found that EPYC1 has five evenly spaced Rubisco-binding
58 regions that share sequence homology and can bind to Rubisco as short peptides. We obtained
59 cryo-electron microscopy structures showing that each of EPYC1's Rubisco-binding regions
60 forms an α -helix that binds one of Rubisco's eight small subunits via salt bridges and hydrophobic
61 interactions. Mapping of these binding sites onto Rubisco holoenzymes within the native pyrenoid
62 matrix indicates that the linker sequences between Rubisco-binding regions on EPYC1 are
63 sufficiently long to connect together adjacent Rubisco holoenzymes. These discoveries advance
64 the understanding of the pyrenoid and provide a high-resolution structural view of a phase-
65 separated organelle.

66

67 **Results**

68

69 We could not directly determine the structure of full-length EPYC1 bound to Rubisco because
70 mixing the two proteins together produces phase-separated condensates¹¹. We thus aimed to first
71 identify Rubisco-binding regions on EPYC1, and subsequently to use a structural approach to
72 determine how these regions bind to Rubisco.

73

74 **EPYC1 has five nearly identical Rubisco-binding regions**

75 The intrinsically disordered nature of purified EPYC1¹¹ led us to hypothesize that the
76 Rubisco-binding regions of EPYC1 were short and could bind to Rubisco as peptides without a
77 need for tertiary folds. Therefore, to identify EPYC1 regions that bind to Rubisco, we synthesized
78 a peptide array consisting of 18 amino acid peptides tiling across the full length EPYC1 sequence
79 (Fig. 1d), and probed this array with native Rubisco purified from *Chlamydomonas* cells (Fig. 1e,
80 f).

81 Our tiling array revealed five evenly-spaced Rubisco-binding regions on EPYC1, each
82 consisting of a predicted α -helix and an upstream region (Fig. 1g, h and Supplementary Table 1).
83 We confirmed the binding regions using surface plasmon resonance (SPR; Extended Data Fig. 1b,
84 c). Sequence alignment guided by the five binding regions revealed that mature EPYC1 consists
85 entirely of five sequence repeats (Fig. 1i), in contrast to the previously defined four repeats and
86 two termini¹⁰ (Extended Data Fig. 1a). Our alignment indicates that the previously defined EPYC1
87 N- and C- termini, which at the time were not considered part of the repeats, actually share
88 sequence homology with the central repeats.

89 The presence of a Rubisco-binding region on each of the previously defined EPYC1 repeats
90 (Extended Data Fig. 1a) explains our yeast two-hybrid observations¹² that a single EPYC1 repeat
91 can interact with Rubisco, that knocking out the α -helix in an EPYC1 repeat disrupts this
92 interaction, and that decreasing the number of EPYC1 repeats leads to a proportional decrease in
93 EPYC1 interaction with Rubisco. It also explains our observations that decreasing the number of
94 EPYC1 repeats leads to a proportional decrease in the tendency of EPYC1 and Rubisco to phase
95 separate together¹¹.

96

97 **EPYC1 binds to Rubisco small subunits**

98 The sequence homology of the five Rubisco-binding regions suggests that each region binds to
99 Rubisco in a similar manner. To identify the binding site of EPYC1 on Rubisco, we determined
100 three structures by using single-particle cryo-electron microscopy. The first structure consists of
101 Rubisco in complex with peptide EPYC1₄₉₋₇₂, representing the first Rubisco-binding region of
102 EPYC1 (2.13 Å overall resolution; ~2.5 Å EPYC1 peptide local resolution; Fig. 2, Extended Data
103 Fig. 2-5; Extended Data Table 1). The second structure consists of Rubisco in complex with a
104 second peptide, EPYC1₁₀₆₋₁₃₅, representing the second, third and fourth Rubisco-binding regions
105 of EPYC1 (2.06 Å overall resolution, ~2.5 Å EPYC1 peptide local resolution, Extended Data Fig.
106 6). The affinities of these peptides to Rubisco were low by protein interaction standards ($K_D \sim 3$
107 mM; Extended Data Fig. 1d, e); thus, millimolar concentrations of peptide were required to
108 approach full occupancy of peptide bound to Rubisco. For reference purposes, we also obtained a
109 third structure of Rubisco in the absence of EPYC1 peptide (2.68 Å; Extended Data Fig. 2 and 3),
110 which was nearly identical to the previously published X-ray crystallography structure¹³, with
111 minor differences likely due to the absence of the substrate analog 2-CABP in the active site of
112 Rubisco in our sample¹⁴ (Extended Data Fig. 4).

113 The structures of Rubisco in complex with EPYC1₄₉₋₇₂ and of Rubisco in complex with
114 EPYC1₁₀₆₋₁₃₅ were remarkably similar, indicating that these two peptides and the corresponding
115 four regions of EPYC1 each bind to the same site on the Rubisco holoenzyme. The Rubisco
116 holoenzyme consists of a core of eight catalytic large subunits in complex with eight small
117 subunits, four of which cap each end of the holoenzyme (Fig. 2b-e). In each structure, an EPYC1
118 peptide was clearly visible bound to each Rubisco small subunit, suggesting that each Rubisco
119 holoenzyme can bind up to eight EPYC1s (Fig. 2b-e and Extended Data Fig. 6b, c).

120

121 **Salt bridges and a hydrophobic interface mediate binding**

122 Both the EPYC1₄₉₋₇₂ and EPYC1₁₀₆₋₁₃₅ peptides formed an extended chain that sits on top of the
123 Rubisco small subunit's two α -helices (Fig. 3a, b, Extended Data Fig. 6d, e). This binding site
124 explains our previous observations that mutations in the Rubisco small subunit α -helices disrupted
125 yeast two-hybrid interactions between EPYC1 and the Rubisco small subunit¹² and prevented
126 Rubisco's assembly into a pyrenoid *in vivo*¹⁵. The C-terminal regions of the EPYC1₄₉₋₇₂ and
127 EPYC1₁₀₆₋₁₃₅ peptides (NW[R/K]QELESLR[N/S]) are well-resolved; each forms an α -helix that
128 runs parallel to helix B of the Rubisco small subunit (Fig. 3a, b). The peptides' N-termini extend

129 the trajectory of the helix and follow the surface of the Rubisco small subunit (Fig. 2b-e, 3a-b and
130 Extended Data Fig. 5, Extended Data Fig. 6b, c). The side chains of the peptides' N-termini could
131 not be well resolved, suggesting that these regions are more conformationally flexible.

132 Our atomic models based on the density maps suggest that binding is mediated by salt
133 bridges and a hydrophobic interface. Three residue pairs of EPYC1₄₉₋₇₂ likely form salt bridges
134 (Fig. 3c, d and g): EPYC1 residues R64 and R71 interact with E24 and D23, respectively, of
135 Rubisco small subunit α -helix A, and EPYC1 residue E66 interacts with R91 of Rubisco small
136 subunit α -helix B. Furthermore, a hydrophobic interface is formed by W63, L67 and L70 of
137 EPYC1 and M87, L90 and V94 of Rubisco small subunit helix B (Fig. 3e-g). Similar interactions
138 were observed for the corresponding residues in EPYC1₁₀₆₋₁₃₅ (Extended Data Fig. 6f-j).

139

140 **Binding and phase separation require interface residues**

141 To determine the importance of individual EPYC1 residues for binding, we investigated the impact
142 on Rubisco binding of every possible single amino acid substitution for EPYC1's first Rubisco-
143 binding region by using a peptide array (Fig. 4a and Supplementary Table 2) and SPR (Extended
144 Data Fig. 7). Consistent with our structural model, the peptide array indicated that EPYC1 salt
145 bridge-forming residues R64, R71 and E66 and the hydrophobic interface residues W63, L67 and
146 L70 were all required for normal EPYC1 binding to Rubisco. The strong agreement of our
147 mutational analysis suggests that our structural model correctly represents EPYC1's Rubisco-
148 binding interface.

149 To determine the importance of EPYC1's Rubisco-binding regions for pyrenoid matrix
150 formation, we assayed the impact of mutations in these regions on formation of phase separated
151 droplets by EPYC1 and Rubisco *in vitro*. The phase boundary was shifted by mutating R64 in the
152 first Rubisco-binding region and the corresponding K or R in the other four Rubisco-binding
153 regions of EPYC1 (Fig. 4b and Extended Data Fig. 8), suggesting that the Rubisco-binding regions
154 mediate condensate formation.

155

156 **Pyrenoid matrix formation requires interface residues**

157 We validated the importance of Rubisco residues for binding to EPYC1 by yeast two-hybrid assays
158 (Fig. 5a and Extended Data Fig. 9). A Rubisco small subunit D23A mutation, which eliminates
159 the charge of the aspartate residue, had a severe impact on Rubisco small subunit interaction with

160 EPYC1, as expected from the contribution of that residue to a salt bridge with R71 and homologous
161 residues of EPYC1's Rubisco-binding regions. Likewise, E24A and R91A each showed a
162 moderate defect, consistent with the contributions of those residues to salt bridges with R64 and
163 E66 (and homologous residues) of EPYC1, respectively. Additionally, M87D and V94D,
164 mutations which convert hydrophobic residues to bulky charged residues, each had a severe impact
165 on interaction, as expected from the participation of those residues in the hydrophobic interface.
166 Combinations of these mutations abolished the interactions completely (Extended Data Fig. 9).

167 To evaluate the importance of the binding interface *in vivo*, we generated *Chlamydomonas*
168 strains with point mutations in the binding interface. Rubisco small subunit mutations D23A/E24A
169 or M87D/V94D caused a growth defect under conditions requiring a functional pyrenoid (Fig. 5b,
170 Extended Data Fig. 10a-b). Furthermore, the mutants lacked a visible pyrenoid matrix (Fig. 5c, d
171 and Extended Data Fig. 10c), indicating that those Rubisco small subunit residues are required for
172 matrix formation *in vivo*. The Rubisco mutants retained pyrenoid tubules¹⁶, as previously observed
173 in other matrix-deficient mutants^{10,17-19}.

174 Together, our data demonstrate that EPYC1's Rubisco-binding regions bind to the Rubisco
175 small subunit α -helices via salt-bridge interactions and a hydrophobic interface, enabling the
176 condensation of Rubisco into the phase separated matrix.

177

178 **A structural model for pyrenoid matrix formation**

179 The presence of multiple Rubisco-binding regions along the EPYC1 sequence supports a model
180 where consecutive Rubisco-binding regions on the same EPYC1 polypeptide can bind to different
181 Rubisco holoenzymes and thus hold them together to form the pyrenoid matrix. If this model is
182 correct, we would expect that the ~40 amino acid "linker" regions between consecutive Rubisco-
183 binding regions on EPYC1 (Fig. 1g, i) would be sufficient to span the distance between EPYC1-
184 binding sites on neighboring Rubisco holoenzymes in the pyrenoid matrix. To test this aspect of
185 the model, we combined our atomic structure of the EPYC1-Rubisco interaction with the precise
186 positions and orientations of Rubisco holoenzymes within the pyrenoid matrix of native cells that
187 we had previously obtained by *in-situ* cryo-electron tomography⁵ (Fig. 6a, b). We mapped the
188 positions of EPYC1 binding sites onto Rubisco holoenzymes in the matrix and measured the
189 distances between nearest neighbor EPYC1 binding sites on adjacent holoenzymes (Fig. 6c,
190 binding sites on the same holoenzyme were excluded in this analysis). The observed distances

191 ranged from ~2 nm to ~7 nm, with a median distance of ~4 nm (Fig. 6d and Supplementary Table
192 3).

193 A “linker” region of 40 amino acids is unlikely to be stretched to its maximum possible
194 length of 14 nm *in vivo* due to the high entropic cost of this configuration. To determine whether
195 a linker region can span the observed distances between nearest neighbor binding sites on adjacent
196 Rubisco holoenzymes, we used a simple physics model to calculate the energy required to stretch
197 a 40 amino acid chain to any given distance (Fig. 6d; see Methods). The model indicates that
198 stretching the chain to ~7 nm requires an energy of $3 k_B T$ (where k_B is the Boltzmann constant and
199 T is the temperature), which could reasonably be derived from thermal fluctuations. Thus, our data
200 suggest that the linker region between consecutive Rubisco-binding sites on the EPYC1
201 polypeptide can span the distance between adjacent Rubisco holoenzymes to hold the pyrenoid
202 matrix together *in vivo*. It also appears likely that, in addition to bridging neighboring Rubisco
203 holoenzymes, consecutive Rubisco-binding regions on a given EPYC1 can bind multiple sites on
204 one Rubisco holoenzyme, as the distance between the nearest binding sites on the same
205 holoenzyme is < 9 nm.

206

207 **Discussion**

208

209 In this study, we have determined the structural basis for pyrenoid matrix formation for the first
210 time in any species. We found that in the model alga *Chlamydomonas*, the intrinsically disordered
211 protein EPYC1 has five regions of similar sequence that can bind to Rubisco as short peptides.
212 These EPYC1 regions form an α -helix that binds to the Rubisco small subunit α -helices via salt
213 bridges and hydrophobic interactions. EPYC1’s Rubisco-binding regions are spaced by linker
214 sequences that are sufficiently long to span the distance between binding sites on adjacent Rubisco
215 holoenzymes within the pyrenoid, allowing EPYC1 to serve as a molecular glue that clusters
216 Rubisco together to form the pyrenoid matrix (Fig. 6e).

217 The multivalency of EPYC1 and the high K_D (~3 mM; Extended Data Fig. 1e) of individual
218 Rubisco-binding regions are consistent with the emerging principle that cellular phase separation
219 is mediated by weak multivalent interactions²⁰. The high dissociation rate constant ($>1/s$; Extended
220 Data Fig. 1d) of individual Rubisco-binding regions explains how the pyrenoid matrix can mix
221 internally on the time scale of seconds⁵ despite the multivalency of EPYC1. The even spacing of

222 the five Rubisco-binding regions across EPYC1 is noteworthy and may be an indication of
223 selective pressure for an optimal distance between binding regions, and thus of an optimal spacing
224 between Rubisco holoenzymes in the matrix.

225 Knowledge of the EPYC1-Rubisco binding mechanism now opens doors to the molecular
226 characterization of the regulation of this interaction, which may govern the dissolution and
227 condensation of the matrix during cell division⁵ and in response to environmental factors²¹. For
228 example, phosphorylation of EPYC1²² may provide a mechanism to rapidly change the binding
229 affinity of EPYC1 to Rubisco. Inactivation of one Rubisco-binding region on EPYC1 would yield
230 four binding regions, which would allow two such EPYC1 molecules (each containing four
231 Rubisco-binding regions, for a total of eight Rubisco-binding regions) to form a mutually satisfied
232 complex with each Rubisco holoenzyme (containing eight EPYC1-binding sites), a configuration
233 that is predicted to favor dissolution of the matrix⁵.

234

235 **Our structures explain how other proteins bind to Rubisco**

236 In a parallel study (Meyer et al., please see unpublished manuscript provided as reference
237 material), we recently discovered that a common sequence motif is present on many pyrenoid-
238 localized proteins. The motif binds Rubisco, enabling recruitment of motif-containing proteins to
239 the pyrenoid and mediating adhesion between the matrix, pyrenoid tubules, and starch sheath. This
240 motif, [D/N]W[R/K]XX[L/I/V/A], is present in EPYC1's Rubisco-binding regions as defined in
241 the present study, and the motif residues mediate key binding interactions with Rubisco. In our
242 structures, the R/K of the motif is represented by R64 and K127 of EPYC1, each of which forms
243 a salt bridge with E24 of the Rubisco small subunit. The XX of the motif almost always includes
244 a D or E; in our structures this feature is represented by E66 and E129 of EPYC1, each of which
245 forms a salt bridge with R91 of the Rubisco small subunit. Finally, the W and [L/I/V/A] of the
246 motif are represented by W63/W126 and L67/L130 of EPYC1, which contribute to the
247 hydrophobic interactions with M87, L90 and V94 of the Rubisco small subunit. The key roles of
248 the motif residues in the interface presented here strongly suggest that the structures we have
249 obtained for motifs from EPYC1 also explain where and how all other variants of the motif,
250 including those found on the key pyrenoid proteins SAGA1, SAGA2, RBMP1, RBMP2 and
251 CSP41A, bind to Rubisco. Our observation that the Rubisco small subunit D23A/E24A and
252 M87D/V94D mutants exhibit a more severe disruption of the pyrenoid than the *epyc1* mutant¹⁰

253 supports the idea that this region of Rubisco interacts not only with EPYC1, but also with other
254 proteins required for pyrenoid biogenesis, making this binding interaction a central hub of
255 pyrenoid biogenesis.

256

257 **Structural differences between the pyrenoid and carboxysomes**

258 Although α - and β -carboxysomes are morphologically, functionally and evolutionarily distinct
259 from the pyrenoid, their Rubisco is also thought to be clustered by linker proteins. Like EPYC1,
260 the α -carboxysome linker protein CsoS2²³ is intrinsically disordered and is proposed to bind
261 Rubisco as an unfolded peptide²⁴. In contrast, the β -carboxysome linker protein CcmM has been
262 proposed to bind Rubisco using folded globular domains^{25,26}. The use of an unfolded peptide as in
263 the case of EPYC1 and CsoS2 may provide the benefit of requiring fewer amino acids for
264 achieving the desired binding function. A notable difference is the location of the binding site on
265 Rubisco: whereas both carboxysomal linker proteins bind to the interface between two Rubisco
266 large subunits^{24,26}, EPYC1 binds to the Rubisco small subunit. It remains to be seen whether this
267 difference in binding site has functional consequences, such as impacts on the three-dimensional
268 packing of Rubisco.

269

270 **Our findings advance the ability to engineer a pyrenoid**

271 There is currently significant interest in engineering Rubisco condensates into monocotyledonous
272 crops such as wheat and rice to enhance yields²⁷⁻³⁰. Binding of EPYC1 to the Rubisco small subunit
273 presents a promising route for engineering a Rubisco condensate, as the Rubisco small subunit is
274 encoded in the nuclear genome, making it more easily amenable to genetic modification in those
275 crops than the chloroplast-encoded Rubisco large subunit³¹. Knowledge of the binding mechanism
276 now allows engineering of minimal sequence changes into native crop Rubiscos to enable binding
277 to EPYC1 and to other key proteins required to reconstitute a functional pyrenoid.

278

279 **Insights into pyrenoid matrix formation in other species**

280 Pyrenoids appear to have evolved independently in different lineages through convergent
281 evolution^{7,32}. EPYC1, its Rubisco-binding sequences, and the amino acid residues that form the
282 EPYC1 binding site on the surface of Rubisco are conserved across the order Volvocales, as
283 evidenced from the genome sequences of *Tetraabaena socialis*, *Gonium pectorale* and *Volvox*

284 *carteri* (Extended Data Table 2). While the molecular mechanisms of matrix formation in other
285 lineages remain to be uncovered, candidate linker proteins have been identified based on similarity
286 of sequence properties to EPYC1¹⁰. We hypothesize that the matrix in other lineages is formed
287 based on similar principles to those we observed in *Chlamydomonas*. Our experimental approach
288 for characterizing the binding interaction provides a roadmap for future structural studies of
289 pyrenoids across the tree of life.

290

291 **We provide a structural view of a phase-separated organelle**

292 The pyrenoid matrix presents an unusual opportunity to study a two-component molecular
293 condensate where one of the components, Rubisco, is large and rigid, and the other component,
294 EPYC1, is a simple intrinsically disordered protein consisting of nearly identical tandem repeats.
295 The rigidity and size of Rubisco holoenzymes previously enabled the determination of their
296 positions and orientations within the pyrenoid matrix of native cells by cryo-electron tomography⁵.
297 The identification of EPYC1 binding sites on Rubisco in the present work and the modeling of
298 linker regions between EPYC1's Rubisco binding regions now make the *Chlamydomonas*
299 pyrenoid matrix one of the most structurally well-defined phase-separated organelles. Thus,
300 beyond advancing our structural understanding of pyrenoids, organelles that play a central role in
301 the global carbon cycle, we hope that the findings presented here will also more broadly enable
302 advances in the biophysical understanding of phase-separated organelles.

303 **Methods**

304

305 **Strains and culture conditions**

306 Chlamydomonas wild-type (WT) strain cMJ030 was maintained in the dark or low light (~10 μmol
307 photons $\text{m}^{-2} \text{s}^{-1}$) on 1.5% agar plates containing Tris-Acetate-Phosphate medium with revised trace
308 elements³³. For Rubisco extraction, 500 mL Tris-Acetate-Phosphate medium in a 1 L flask was
309 inoculated with a loopful of cells and the culture was grown to 4×10^6 cells/mL at 22°C, shaking
310 at 200 rpm under ~100 μmol photons $\text{m}^{-2} \text{s}^{-1}$ white light in 3% CO₂. Chlamydomonas mutant T60-
311 3³⁴ (*ΔrbcS*; containing a deletion of both *RBCS* genes) was used for generating Rubisco small
312 subunit point mutants and a wild-type control in the same background. This strain was maintained
313 on agar in the dark or low light (~10 μmol photons $\text{m}^{-2}\text{s}^{-1}$).

314

315 **Protein extraction**

316 Rubisco was purified from Chlamydomonas strain cMJ030³⁵. Cells were disrupted by
317 ultrasonication in lysis buffer (10 mM MgCl₂, 50 mM Bicine, 10 mM NaHCO₃, 1 mM
318 dithiothreitol, pH 8.0) supplemented with Halt Protease Inhibitor Cocktail, EDTA-Free (Thermo
319 Fisher Scientific). The soluble lysate was fractionated by ultracentrifugation on a 10-30% sucrose
320 gradient in a SW 41 Ti rotor at a speed of 35,000 rpm for 20 hours at 4°C. Rubisco-containing
321 fractions were applied to an anion exchange column (MONO Q 5/50 GL, GE Healthcare) and
322 eluted with a linear salt gradient from 30 to 500 mM NaCl in lysis buffer.

323

324 **Peptide arrays**

325 Peptide arrays were purchased from the MIT Biopolymers Laboratory (Cambridge, MA). The
326 tiling array was composed of 18-amino-acid peptides that tiled across the full-length EPYC1
327 sequence with a step size of one amino acid. Each peptide was represented by at least two spots
328 on the array, and these replicates were averaged during data analysis. The locations of peptides on
329 the array were randomized. In the substitution arrays, peptides were designed to represent every
330 possible one-amino-acid mutation of the indicated region on EPYC1 by substitution with one of
331 the other 19 amino acids. The arrays were activated by methanol, then washed 3x10 min in binding
332 buffer (50 mM HEPES, 50 mM KOAc, 2 mM Mg(OAc)₂·4H₂O, 1 mM CaCl₂ and 200 mM sorbitol,
333 pH 6.8). The arrays were then incubated at 4°C with 1 mg purified Rubisco overnight. The arrays

334 were washed in binding buffer to remove any unbound Rubisco. Using a semi-dry transfer
335 apparatus (BIO-RAD), bound Rubisco was transferred onto an Immobilon-P PVDF membrane
336 (Millipore Sigma). The Rubisco was detected by one of two methods: western blotting, or
337 fluorescent labeling. While replicates using the two methods gave similar results, toward the end
338 of the project we found that fluorescent labeling had a lower background, so we show fluorescent
339 labeling data in Figure 1; all other data were obtained by western blotting and chemiluminescence.
340 For fluorescent labeling, Rubisco was labeled with Alexa Fluor™ 680 dye (Thermo Fisher
341 Scientific) and detected by Typhoon Scanner (GE Healthcare). For western blotting, Rubisco was
342 immuno-detected with a polyclonal primary antibody raised against Rubisco¹⁵ (1:10,000) followed
343 by a HRP conjugated goat anti-rabbit (1:20,000; Invitrogen), and the chemiluminescence was
344 detected by ImageQuant LAS 4000 (GE Healthcare). Images were analyzed with ImageQuant TL
345 (GE Healthcare). Arrays were stripped with Restore™ Western Blot Stripping Buffer before re-
346 use (Thermo Fisher Scientific).

347 For both types of arrays, values for identical sequences present multiple times were
348 averaged. For tiling arrays, the average value for each sequence was plotted at its position in
349 EPYC1 (or at multiple positions for sequences present multiple times). For amino acid substitution
350 arrays, the ratio of each substitution sequence to the corresponding wildtype sequence was
351 calculated and arrayed by amino acid and position.

352

353 **Surface plasmon resonance (SPR) experiments**

354 All the surface preparation experiments were performed at 25°C using a Biacore 3000 instrument
355 (GE Healthcare). Purified Rubisco was immobilized on CM5 sensor chips using a Biacore Amine
356 Coupling Kit according to the manufacturer's instructions. Briefly, the chip surface was activated
357 by an injection of 1:1 N-hydroxysuccinimide (NHS)/1-ethyl-3-(3-
358 dimethylaminopropyl)carbodiimide hydrochloride (EDC). Rubisco was diluted to ~100 µg/mL in
359 10 mM acetate (pH 4.5; this pH had been previously optimized using the immobilization pH
360 scouting wizard) and was injected over the chip surface. Excess free amine groups were then
361 capped with an injection of 1 M ethanolamine. Typical immobilization levels were 8,000 to 10,000
362 resonance units (RU), as recommended for binding experiments of small molecules. For kinetic
363 experiments (for determining the binding affinities), the typical immobilization levels were ~5,000
364 RU. The control surfaces were prepared in exactly the same manner as the experimental surfaces

365 except that no Rubisco was injected. For immobilizations, the running buffer was the Biacore
366 HBS-EP Buffer (0.01 M HEPES pH 7.4, 0.15 M NaCl, 3 mM EDTA, 0.005% v/v Surfactant P20).

367 All the binding assays were performed using the Biacore PBS-P+ Buffer (20 mM
368 phosphate buffer, 2.7 mM KCl, 137 mM NaCl and 0.05% Surfactant P20, pH 6.8) as a running
369 buffer, as recommended for small molecule analysis in Biacore systems. The analytes, consisting
370 of EPYC1 peptides synthesized by Genscript (Piscataway, New Jersey), were dissolved in the
371 same running buffer and diluted to 1 mM. The analytes were injected over the control surface and
372 experimental surfaces at a flow rate of 26 $\mu\text{L}/\text{min}$ for 2.5 minutes, followed by 2.5 minutes of the
373 running buffer alone to allow for dissociation. The surfaces were then regenerated using running
374 buffer at a flow rate of 30 $\mu\text{L}/\text{min}$ for 10 minutes. In all cases, binding to the control surface was
375 negligible.

376 For determining the K_D of EPYC1 peptide, the kinetic assays were performed with a
377 running buffer consisting of 200 mM sorbitol, 50 mM HEPES, 50 mM KOAc, 2 mM
378 $\text{Mg}(\text{OAc})_2 \cdot 4\text{H}_2\text{O}$ and 1 mM CaCl_2 at pH 6.8 (the same buffer as the peptide array assay). The
379 EPYC1 peptide was dissolved in the same running buffer as the assay and the serial dilutions were
380 also made in the same buffer. The analytes were injected over the control surface and experimental
381 surfaces at a flow rate of 15 $\mu\text{L}/\text{min}$ for 2 minutes, followed by 10 minutes with the running buffer
382 alone to allow for dissociation. The surfaces were then regenerated by the running buffer at a flow
383 rate of 30 $\mu\text{L}/\text{min}$ for 10 minutes. In all cases, binding to the blank chip was negligible. The fitting
384 and modeling were performed with the BIAevaluation software.

385

386 **Single-particle cryo-electron microscopy data collection and image processing**

387 Rubisco and EPYC1₄₉₋₇₂ peptides with the final concentrations of 1.69 mg/ml (=3.02 μM) and 7.5
388 mM, respectively, were incubated together on ice for 20 minutes in buffer consisting of 200 mM
389 sorbitol, 50 mM HEPES, 50 mM KOAc, 2 mM $\text{Mg}(\text{OAc})_2 \cdot 4\text{H}_2\text{O}$ and 1 mM CaCl_2 at pH 6.8 (the
390 same buffer as the peptide array assay and the SPR binding assay). Rubisco and EPYC1₁₀₆₋₁₃₅
391 peptides with the final concentrations of 1.75 mg/ml (=3.13 μM) and 10 mM, respectively, were
392 incubated together on ice for 20 minutes in the same buffer described above. For apo Rubisco and
393 Rubisco incubated with peptides, similar cryo grid-making procedures were used. 400-mesh
394 Quantifoil 1.2/1.3 Cu grids (Quantifoil, Großlobichau, Germany) were made hydrophilic by glow
395 discharging for 60 seconds with a current of 15 mA in a PELCO easiGlow system. Cryo grids

396 were produced using a FEI Mark IV Vitrobot (FEI company, part of Thermo Fisher Scientific,
397 Hillsboro, OR). The chamber of the Vitrobot was kept at 4°C and 100% relative humidity. 3 µl of
398 sample was applied to the glow-discharged grid and blotted with filter paper for 3 seconds with
399 the equipment-specific blotting force set at 3. After blotting, the grid was rapidly plunge-frozen
400 into a liquid ethane bath.

401 For apo Rubisco and Rubisco incubated with EPYC1₄₉₋₇₂ peptide, cryo grids were loaded
402 into a 300 kV FEI Titan Krios cryo electron microscope (FEI Company) at HHMI Janelia Research
403 Campus, Janelia Krios2, equipped with a Gatan K2 Summit camera. After initial screening and
404 evaluation, fully automated data collection was carried out using SerialEM. The final exposure
405 from each collection target was collected as a movie utilizing dose fractionation on the K2 Summit
406 camera operated in super-resolution mode. The movies were collected at a calibrated magnification
407 of 38,168x, corresponding to 1.31 Å per physical pixel in the image (0.655 Å per super-resolution
408 pixel). The dose rate on the specimen was set to be 5.82 electrons per Å² per second and total
409 exposure time was 10 s, resulting in a total dose of 58.2 electrons per Å². With dose fractionation
410 set at 0.2 s per frame, each movie series contained 50 frames and each frame received a dose of
411 1.16 electrons per Å². The spherical aberration constant of the objective lens is 2.7 mm and an
412 objective aperture of 100 µm was used. The nominal defocus range for the automated data
413 collection was set to be between -1.5 µm and -3.0 µm. For Rubisco incubated with EPYC1₁₀₆₋₁₃₅
414 peptide, the final exposure was collected on Janelia Krios1 equipped with a Cs-corrector, a Gatan
415 Bioquantum energy filter and a post-filter K3 camera. The movies were collected at a nominal
416 magnification of 81,000x, corresponding to 0.844 Å per physical pixel in the image (0.422 Å per
417 super-resolution pixel). The dose rate on the specimen was set to be 12 electrons per pixel per
418 second and total exposure time was 3.56 s, resulting in a total dose of 60 electrons per Å². Each
419 movie series contained 60 frames and each frame received a dose of 1 electron per Å². The nominal
420 defocus range for the automated data collection was set to be between -1 µm and -1.6 µm.

421 The movies were 2x binned and motion corrected using MotionCor2³⁶ and CTF was
422 estimated using CTFFIND³⁷ in Relion³⁸. 1,809,869 EPYC1₄₉₋₇₂ peptide-bound Rubisco particles,
423 2,257,131 EPYC1₁₀₆₋₁₃₅ peptide-bound Rubisco particles, and 677,071 Rubisco particles in the apo
424 state were selected using cisTEM³⁹. 2D classification was performed using cisTEM. The classes
425 presenting detailed features in class averages were chosen for 3D classification on cryoSPARC^{40,41}
426 and on Relion. The 3D class showing clear secondary structures was chosen for 3D auto-refine

427 first without symmetry and then with D4 symmetry imposed. After CTF refinement and Bayesian
428 polishing in Relion, the reconstructed map resolution is 2.68 Å for the apo state, 2.62 Å for the
429 EPYC1₄₉₋₇₂ peptide-bound state, and 2.06 Å for the EPYC1₁₀₆₋₁₃₅ peptide-bound state. The
430 EPYC1₄₉₋₇₂ peptide-bound particles at super-resolution pixel size were further subjected to CTF
431 refinement and polishing, resulting in map at 2.13 Å resolution. Details for single-particle cryo-
432 EM data collection and image processing are included in the Extended Data Table 1.

433

434 **Single-particle cryo-electron microscopy model building, fitting, and refinement**

435 A full model for Rubisco from *Chlamydomonas* was produced from an X-ray structure¹³ (PDB
436 entry 1GK8) and used for rigid body fitting into a local resolution filtered apo or EPYC1₄₉₋₇₂
437 peptide-bound Rubisco cryo-EM map using UCSF Chimera⁴². After rigid body fitting of the full
438 complex, initial flexible fitting was performed in COOT⁴³ by manually going through the entire
439 peptide chain of a single large and small Rubisco subunit before applying the changes to the other
440 seven large and small subunits. The C-terminal part of the small subunit was built manually and
441 the sequences updated to the RBCS2 sequences. The sequence of the EPYC1₄₉₋₇₂ peptide was used
442 to predict secondary structure elements using JPred4⁴⁴, which gave the prediction that the C-
443 terminal region (NWRQELES) is α -helical. Guided by this prediction, the peptide was built
444 manually into the density using COOT. Additional maps like the initial 2.62 Å from the binned
445 data and maps filtered to different resolutions with various applied B-factors were also used to
446 help with model building in unclear regions. Additional real space refinement of the entire complex
447 was performed using Phenix⁴⁵. The EPYC1₁₀₆₋₁₃₅ peptide bound map was used to build a model of
448 the EPYC1₁₀₆₋₁₃₅ peptide. First rigid body fitting of the EPYC1₄₉₋₇₂ peptide-bound Rubisco model
449 into a local resolution filtered EPYC1₁₀₆₋₁₃₅ peptide-bound Rubisco cryo-EM map was performed
450 using UCSF Chimera. Then the sequence of the peptide was mutated to the EPYC1₁₀₆₋₁₃₅ peptide
451 sequence, followed by flexible fitting to slightly adjust the PDB to the density. Models were
452 subjected to an all-atom structure validation using MolProbity⁴⁶. Figures were produced using
453 UCSF Chimera.

454

455 **Liquid–liquid phase separation assay**

456 Proteins used in the liquid–liquid phase separation assay were obtained and stored essentially as
457 described previously¹¹. Briefly, Rubisco was purified from *Chlamydomonas reinhardtii* cells (CC-

458 2677 cw15 nit1-305 mt-5D, Chlamydomonas Resource Center), grown in Sueoka's high-salt
459 medium⁴⁷, using a combination of anion exchange chromatography and gel filtration.

460 The EPYC1 full-length gene (encoding amino acids 1-317) and corresponding R/K mutant
461 (EPYC1^{R64A/K127A/K187A/K248A/R314A}) were synthesized by GenScript and cloned between the SacII
462 and HindIII site of the pHue vector⁴⁸. Proteins were produced in the *E. coli* strain BL21 (DE3)
463 harbouring pBADESL⁴⁹ for co-expression of the *E. coli* chaperonin GroEL/S. The purification
464 was conducted with minor changes (dialysis for removal of high imidazol concentrations was
465 skipped by running the gel-filtration column before the second IMAC). After the first IMAC step
466 and cleavage⁵⁰ of the N-terminal His₆-ubiquitin tag, proteins were separated by gel filtration.
467 Finally, the peak fraction was passed a second time through an IMAC column, collecting EPYC1
468 from the flow through.

469 EPYC1-Rubisco condensates were reconstituted *in vitro* in a buffer containing 20 mM
470 Tris-HCl (pH 8.0) and NaCl concentrations as indicated. 5 µl reactions were incubated for 3
471 minutes at room temperature before monitoring the droplet formation by differential interference
472 contrast (DIC) microscopy. DIC images were acquired with a Nikon Eclipse Ti Inverted
473 Microscope using a 60× oil-immersion objective after allowing the droplets to settle on the
474 coverslip (Superior Marienfeld, Germany) surface for about 3 minutes. For droplet sedimentation
475 assays 10 µl reactions were incubated for 3 minutes at 20°C before separating the droplets from
476 the bulk phase by spinning for 3 minutes at 21,000xg and 4°C. Pelleted droplets and supernatant
477 fractions were analyzed using Coomassie-stained SDS-PAGE.

478

479 **Yeast two-hybrid assay**

480 Yeast two-hybrid to detect interactions between EPYC1 and RbcS1 was carried out as described
481 previously¹². EPYC1 was cloned into the two-hybrid vector pGBKT7 to create a fusion with the
482 GAL4 DNA binding domain. Point mutations were introduced by PCR into RbcS1, which was
483 then cloned in the pGADT7 to create a fusion with the GAL4 activation domain. Yeast cells were
484 then co-transformed with binding and activation domain vectors. Successful transformants were
485 cultured, diluted to an optical density at 600 nm (OD₆₀₀) of 0.5 or 0.1, and plated onto SD-L-W
486 and SD-L-W-H containing increasing concentrations of the HIS3 inhibitor triaminotriazole (3-
487 AT). Plates were imaged after 3 days. Spots shown in Fig. 5a were grown at 5 mM 3-AT from a
488 starting OD₆₀₀ of 0.5; they are a subset of the full dataset shown in Extended Data Fig. 6.

489

490 **Cloning of Rubisco small subunit point mutants**

491 The plasmid pSS1-ITP⁵¹ which contains *Chlamydomonas RBCS1* including UTRs and introns 1
492 and 2 was used as a starting point for generating plasmids pSH001 and pSH002, which encode
493 *RBCS1*^{D23A/E24A}, and *RBCS1*^{M87D/V94D}, respectively. The point mutations were generated by
494 Gibson assembly⁵² of gBlocks (synthesized by Integrated DNA Technologies) containing the
495 desired mutations into pSS-ITP that had been enzyme digested by restriction endonucleases (XcmI
496 and BbvCI for the D23A/E24A mutations and BbvCI and BlnI for the M87D/V94D mutations).
497 All constructs were verified by Sanger sequencing.

498 The fragment for making pSH001 (containing the D23A/E24A Rubisco small subunit
499 mutant) had the following sequence:

500 GCAGGGCTGCCCCGGCTCAGGCCAACCAGATGATGGTCTGGACCCCGGTCAACAAC
501 AAGATGTTTCGAGACCTTCTCCTACCTGCCTCCTCTGACCGCCGCGCAGATCGCCGCC
502 CAGGTCGACTACATCGTCGCCAACGGCTGGATCCCCTGCCTGGAGTTCGCTGAGGCC
503 GACAAGGCCTACGTGTCCAAC

504 The fragment for making pSH002 (containing the M87D/V94D Rubisco small subunit
505 mutant) had the following sequence:

506 CTGCCTGGAGTTCGCTGAGGCCGACAAGGCCTACGTGTCCAACGAGTCGGCCATCC
507 GCTTCGGCAGCGTGTCTTGCCTGTACTACGACAACCGCTACTGGACCATGTGGAAGC
508 TGCCCATGTTTCGGCTGCCGCGACCCCGACCAGGTGCTGCGCGAGATCGACGCCTGCA
509 CCAAGGCCTTCCCCGATGCCTACGTGCGCCTGGTGGCCTTCGACAACCAGAAGCAG
510 GTGCAGATCATGGGCTTCTGGTCCAGCGCCCCAAGACTGCCCGCGACTTCCAGCCC
511 GCCAACAAGCGCTCCGTGTAAATGGAGGCGCTCGTCGATCTGAGCCGTGTGTGATGT
512 TTGTTGGTGTGTTGAGCGAGTGCAATGAGAGTGTGTGTGTGTGTGTTGTTGGTGTGTG
513 GCTAAGCCAAGCGTGATCGC

514 Both the plasmids pSH001 and pSH002 have been submitted to the *Chlamydomonas*
515 Resource Center (www.chlamycollection.org).

516

517 **Transformation of *Chlamydomonas* to make the Rubisco small subunit point mutants**

518 *Chlamydomonas* strains $\Delta rbcS;RBCS^{WT}$, $\Delta rbcS;RBCS^{D23A/E24A}$, and $\Delta rbcS;RBCS^{M87D/V94D}$ (The
519 accession numbers of these strains in *Chlamydomonas* Resource Center are CC-5616, CC-5617

520 and CC-5618, respectively.) were generated by transforming pSS1-ITP, pSH001, and pSH002
521 (encoding Rubisco small subunit constructs) into the Rubisco small subunit deletion mutant T60
522 (*Arbcs*) by electroporation as described previously⁵³. For each transformation, 29 ng kbp⁻¹ of KpnI
523 linearized plasmid was mixed with 250 μ L of 2×10^8 cells mL⁻¹ at 16°C and electroporated
524 immediately. Transformant colonies were selected on Tris-Phosphate plates without antibiotics at
525 3% v/v CO₂ under ~ 50 μ mol photons m⁻² s⁻¹ light. The sequence of RbcS in the transformants was
526 verified by PCR amplification and Sanger sequencing.

527

528 **Spot tests**

529 *Arbcs;RBCS^{WT}*, *Arbcs;RBCS^{D23A/E24A}*, and *Arbcs;RBCS^{M87D/V94D}* (The accession numbers of these
530 strains in Chlamydomonas Resource Center are CC-5616, CC-5617 and CC-5618, respectively.)
531 were grown in Tris-Phosphate medium at 3% CO₂ until $\sim 2 \times 10^6$ cells mL⁻¹. Cells were diluted in
532 Tris-Phosphate medium to a concentration of 8.7×10^7 cells mL⁻¹, then serially diluted 1:10 three
533 times. 7.5 μ L of each dilution was spotted onto four TP plates and incubated in air or 3% CO₂
534 under 20 or 100 μ mol photons m⁻² s⁻¹ white light for 9 days before imaging.

535

536 **Transmission electron microscopy**

537 Samples for electron microscopy were fixed for 1 hour at room temperature in 2.5% glutaraldehyde
538 in Tris-Phosphate medium (pH 7.4), followed by 1 hour at room temperature in 1% OsO₄, 1.5%
539 K₃Fe(CN)₃, and 2 mM CaCl₂. Fixed cells were then bulk stained for 1 hour in 2% uranyl acetate,
540 0.05 M maleate buffer at pH 5.5. After serial dehydration (50%, 75%, 95%, and 100% ethanol,
541 followed by 100% acetonitrile), samples were embedded in epoxy resin containing 34% Quetol
542 651, 44% nonenyl succinic anhydride, 20% methyl-5- norbornene-2,3-dicarboxylic anhydride, and
543 2% catalyst dimethylbenzylamine. Ultramicrotomy was done by the Core Imaging Lab, Medical
544 School, Rutgers University. Imaging was performed at the Imaging and Analysis Center, Princeton
545 University, on a CM100 transmission electron microscope (Philips, Netherlands) at 80 kV.

546

547 **Measurement of nearest-neighbor distances between EPYC1 binding sites on Rubisco** 548 **holoenzymes within pyrenoids**

549 For detailed descriptions of the Chlamydomonas cell culture, vitrification of cells onto EM grids,
550 thinning of cells by cryo-focused ion beam milling, 3D imaging of native pyrenoids by cryo-

551 electron tomography, tomographic reconstruction, template matching, and subtomogram
552 averaging, see our previous study⁵. In that study, we measured the distances between the center
553 positions of Rubisco complexes within tomograms of five pyrenoids. The spatial parameters
554 determined in that study were combined with the EPYC1-binding sites resolved here by cryo-EM
555 single-particle analysis to measure the nearest-neighbor distances between EPCY1 binding sites
556 on adjacent Rubisco complexes within the native pyrenoid matrix.

557 The *in situ* subtomogram average EMD-3694⁵ was used as the reference for the Rubisco
558 model. We extracted the isosurface from this density using the 0.5 contour level recommended in
559 the Electron Microscopy Data Bank entry. We then fit the atomic model of EPYC1-bound Rubisco
560 (Fig. 2) within the EMD-3694 density, and for each EPYC1 binding site, we marked the closest
561 point on the isosurface to define the EPYC1 binding sites on this model. The positions and
562 orientations previously determined by subtomogram averaging were used to place each Rubisco
563 model and its corresponding binding sites into the pyrenoid tomograms using the PySeg program⁵⁴.

564 To compute the nearest-neighbor distances between EPYC1 binding sites on two different
565 Rubisco complexes, first, linkers were drawn between each EPYC1 binding site and all other
566 binding sites within 25 nm. Binding sites on the same Rubisco complex were ignored. Next, the
567 linkers were filtered by length (defined as the Euclidean distance between the two binding sites),
568 and only the shortest linker was retained for each binding site. To prevent edge effects, linkers
569 were discarded if they had a binding site <12 nm from the masked excluded volume (grey in Fig.
570 6b), which marks the border of the analyzed pyrenoid matrix. Finally, linker distances were plotted
571 in a histogram to show the distribution of lengths (normalized to 100%).

572 Regarding the accuracy of the Rubisco localization in the previous study⁵, we used
573 template matching, subtomogram alignment, and hierarchical classification to identify 97.5% of
574 the Rubisco complexes in each of the five pyrenoid volumes. The Rubisco average was determined
575 at a resolution of 16.5 Å. This could be interpreted to mean that the Rubisco complexes were
576 localized with 1.65 nm precision. However, this resolution is not a simple reflection of translational
577 and rotational accuracy, but is also greatly limited by the contrast transfer function and pixel size
578 of the tomographic data. Furthermore, with this localization uncertainty being random for each
579 particle, it would not change the ~4 nm peak distance between neighboring EPYC1 binding sites
580 measured in our current study.

581

582 **Modeling of the energy required to stretch EPYC1-linker regions**

583 The energy required to stretch the linker regions between EPYC1's Rubisco-binding regions was
584 determined as follows. The force F required to stretch a 40 amino acid linker region to any given
585 length z was approximated using a wormlike chain model⁵⁵:

586
$$F(z) = \frac{k_B T}{4L_p} \left[\frac{1}{(1 - z/L_0)^2} - 1 + \frac{4z}{L_0} \right]$$

587 In the above equation, k_B is the Boltzmann constant, T is the temperature, L_p is the persistence
588 length (assumed to be 1 nm, a representative value for disordered proteins), and L_0 is the contour
589 length (estimated as 40 amino acids * 0.36 nm/amino acid). The energy required to stretch the
590 linker to a length x is given by:

591
$$E(x) = \int_0^x F(z) dz$$

592 This energy was calculated and plotted in Fig. 6d.

593

594 **Data availability**

595 All data generated or analyzed during this study are included in this Article, the Extended Data
596 and the Supplementary tables. The single-particle cryo-EM maps have been deposited in the
597 Electron Microscopy Data Bank with accession codes EMDB-22401, EMDB-22308 and EMDB-
598 22462. The atomic models have been deposited in the Protein Data Bank under accession codes
599 PDB 7JN4, PDB 7JFO and PDB 7JSX. The raw datasets have been deposited in the Electron
600 Microscopy Public Image Archive with accession codes EMPIAR-10503, EMPIAR-10502 and
601 EMPIAR-10501. The subtomogram average of Rubisco has been deposited in the Electron
602 Microscopy Data Bank with accession code EMD-3694.

603

604 **References**

- 605 1 Field, C. B., Behrenfeld, M. J., Randerson, J. T. & Falkowski, P. Primary production of the
606 biosphere: integrating terrestrial and oceanic components. *Science* **281**, 237-240 (1998).
- 607 2 Hessler, A. M., Lowe, D. R., Jones, R. L. & Bird, D. K. A lower limit for atmospheric
608 carbon dioxide levels 3.2 billion years ago. *Nature* **428**, 736-738 (2004).
- 609 3 Ainsworth, E. A. & Long, S. P. What have we learned from 15 years of free-air CO₂
610 enrichment (FACE)? A meta-analytic review of the responses of photosynthesis, canopy
611 properties and plant production to rising CO₂. *New Phytol* **165**, 351-371,
612 doi:10.1111/j.1469-8137.2004.01224.x (2005).
- 613 4 Raven, J. A., Cockell, C. S. & De La Rocha, C. L. The evolution of inorganic carbon
614 concentrating mechanisms in photosynthesis. *Philosophical transactions of the Royal
615 Society of London. Series B, Biological sciences* **363**, 2641-2650,
616 doi:10.1098/rstb.2008.0020 (2008).
- 617 5 Freeman Rosenzweig, E. S. *et al.* The Eukaryotic CO₂-Concentrating Organelle Is Liquid-
618 like and Exhibits Dynamic Reorganization. *Cell* **171**, 148-162 e119,
619 doi:10.1016/j.cell.2017.08.008 (2017).
- 620 6 Badger, M. R. *et al.* The diversity and coevolution of Rubisco, plastids, pyrenoids, and
621 chloroplast-based CO₂-concentrating mechanisms in algae. *Can J Bot* **76**, 1052–1071,
622 doi:10.1139/b98-074 (1998).
- 623 7 Villarreal, J. C. & Renner, S. S. Hornwort pyrenoids, carbon-concentrating structures,
624 evolved and were lost at least five times during the last 100 million years. *Proc Natl Acad
625 Sci U S A* **109**, 18873-18878, doi:10.1073/pnas.1213498109 (2012).
- 626 8 Wang, Y., Stessman, D. J. & Spalding, M. H. The CO₂ concentrating mechanism and
627 photosynthetic carbon assimilation in limiting CO₂ : how Chlamydomonas works against
628 the gradient. *The Plant journal : for cell and molecular biology* **82**, 429-448,
629 doi:10.1111/tpj.12829 (2015).
- 630 9 Raven, J. A. CO₂-concentrating mechanisms: A direct role for thylakoid lumen
631 acidification? *Plant Cell Environ* **20**, 147-154, doi:Doi 10.1046/J.1365-3040.1997.D01-
632 67.X (1997).
- 633 10 Mackinder, L. C. *et al.* A repeat protein links Rubisco to form the eukaryotic carbon-
634 concentrating organelle. *Proc Natl Acad Sci U S A* **113**, 5958-5963,
635 doi:10.1073/pnas.1522866113 (2016).
- 636 11 Wunder, T., Cheng, S. L. H., Lai, S. K., Li, H. Y. & Mueller-Cajar, O. The phase separation
637 underlying the pyrenoid-based microalgal Rubisco supercharger. *Nature communications*
638 **9**, 5076, doi:10.1038/s41467-018-07624-w (2018).

- 639 12 Atkinson, N. *et al.* The pyrenoidal linker protein EPYC1 phase separates with hybrid
640 Arabidopsis-Chlamydomonas Rubisco through interactions with the algal Rubisco small
641 subunit. *Journal of experimental botany* **70**, 5271-5285, doi:10.1093/jxb/erz275 (2019).
- 642 13 Taylor, T. C., Backlund, A., Bjorhall, K., Spreitzer, R. J. & Andersson, I. First crystal
643 structure of Rubisco from a green alga, *Chlamydomonas reinhardtii*. *J Biol Chem* **276**,
644 48159-48164, doi:10.1074/jbc.M107765200 (2001).
- 645 14 Duff, A. P., Andrews, T. J. & Curmi, P. M. The transition between the open and closed
646 states of rubisco is triggered by the inter-phosphate distance of the bound bisphosphate. *J*
647 *Mol Biol* **298**, 903-916, doi:10.1006/jmbi.2000.3724 (2000).
- 648 15 Meyer, M. T. *et al.* Rubisco small-subunit α -helices control pyrenoid formation in
649 *Chlamydomonas*. *Proc Natl Acad Sci U S A* **109**, 19474-19479,
650 doi:10.1073/pnas.1210993109. (2012).
- 651 16 Engel, B. D. *et al.* Native architecture of the *Chlamydomonas* chloroplast revealed by in
652 situ cryo-electron tomography. *eLife* **4**, DOI: 10.7554/eLife.04889,
653 doi:10.7554/eLife.04889 (2015).
- 654 17 Goodenough, U. W. & Levine, R. P. Chloroplast structure and function in ac-20, a mutant
655 strain of *Chlamydomonas reinhardtii*. 3. Chloroplast ribosomes and membrane organization.
656 *J Cell Biol.* **44**, 547-562, doi:10.1083/jcb.44.3.547 (1970).
- 657 18 Ma, Y., Pollock, S. V., Xiao, Y., Cunnusamy, K. & Moroney, J. V. Identification of a novel
658 gene, CIA6, required for normal pyrenoid formation in *Chlamydomonas reinhardtii*. *Plant*
659 *Physiol* **156**, 884-896, doi:10.1104/pp.111.173922 (2011).
- 660 19 Caspari, O. D. *et al.* Pyrenoid loss in *Chlamydomonas reinhardtii* causes limitations in CO₂
661 supply, but not thylakoid operating efficiency. *Journal of experimental botany* **68**, 3903-
662 3913, doi:10.1093/jxb/erx197 (2017).
- 663 20 Li, P. *et al.* Phase transitions in the assembly of multivalent signalling proteins. *Nature*
664 **483**, 336-340, doi:10.1038/nature10879 (2012).
- 665 21 Borkhsenius, O. N., Mason, C. B. & Moroney, J. V. The Intracellular Localization of
666 Ribulose-1,5-Bisphosphate Carboxylase/Oxygenase in *Chlamydomonas reinhardtii*. *Plant*
667 *Physiol* **116**, 1585-1591, doi:10.1104/pp.116.4.1585 (1998).
- 668 22 Turkina, M. V., Blanco-Rivero, A., Vainonen, J. P., Vener, A. V. & Villarejo, A. CO₂
669 limitation induces specific redox-dependent protein phosphorylation in *Chlamydomonas*
670 *reinhardtii*. *Proteomics* **6**, 2693-2704, doi:10.1002/pmic.200500461 (2006).
- 671 23 Cai, F. *et al.* Advances in Understanding Carboxysome Assembly in *Prochlorococcus* and
672 *Synechococcus* Implicate CsoS2 as a Critical Component. *Life (Basel)* **5**, 1141-1171,
673 doi:10.3390/life5021141 (2015).

- 674 24 Oltrogge, L. M. *et al.* Multivalent interactions between CsoS2 and Rubisco mediate alpha-
675 carboxysome formation. *Nat Struct Mol Biol* **27**, 281-287, doi:10.1038/s41594-020-0387-
676 7 (2020).
- 677 25 Long, B. M., Badger, M. R., Whitney, S. M. & Price, G. D. Analysis of carboxysomes
678 from *Synechococcus* PCC7942 reveals multiple Rubisco complexes with carboxysomal
679 proteins CcmM and CcaA. *J Biol Chem* **282**, 29323-29335, doi:10.1074/jbc.M703896200
680 (2007).
- 681 26 Wang, H. *et al.* Rubisco condensate formation by CcmM in beta-carboxysome biogenesis.
682 *Nature* **566**, 131-135, doi:10.1038/s41586-019-0880-5 (2019).
- 683 27 Hennacy, J. H. & Jonikas, M. C. Prospects for Engineering Biophysical CO₂ Concentrating
684 Mechanisms into Land Plants to Enhance Yields. *Annual review of plant biology*,
685 doi:10.1146/annurev-arplant-081519-040100 (2020).
- 686 28 Long, B. M. *et al.* Carboxysome encapsulation of the CO₂-fixing enzyme Rubisco in
687 tobacco chloroplasts. *Nature communications* **9**, 3570, doi:10.1038/s41467-018-06044-0
688 (2018).
- 689 29 Lin, M. T., Occhialini, A., Andralojc, P. J., Parry, M. A. & Hanson, M. R. A faster Rubisco
690 with potential to increase photosynthesis in crops. *Nature* **513**, 547-550,
691 doi:10.1038/nature13776 (2014).
- 692 30 Atkinson, N. *et al.* Introducing an algal carbon-concentrating mechanism into higher
693 plants: location and incorporation of key components. *Plant Biotechnol J* **14**, 1302-1315,
694 doi:10.1111/pbi.12497 (2016).
- 695 31 Hanson, M. R., Gray, B. N. & Ahner, B. A. Chloroplast transformation for engineering of
696 photosynthesis. *Journal of experimental botany* **64**, 731-742, doi:10.1093/jxb/ers325
697 (2013).
- 698 32 Raven, J. A., Beardall, J. & Sanchez-Baracaldo, P. The possible evolution and future of
699 CO₂-concentrating mechanisms. *J Exp Bot* **68**, 3701-3716, doi:10.1093/jxb/erx110 (2017).
- 700 33 Kropat, J. *et al.* A revised mineral nutrient supplement increases biomass and growth rate
701 in *Chlamydomonas reinhardtii*. *The Plant journal : for cell and molecular biology* **66**, 770-
702 780, doi:10.1111/j.1365-313X.2011.04537.x (2011).
- 703 34 Khrebtukova, I. & Spreitzer, R. J. Elimination of the *Chlamydomonas* gene family that
704 encodes the small subunit of ribulose-1,5-bisphosphate carboxylase/oxygenase. *Proc Natl*
705 *Acad Sci U S A* **93**, 13689–13693, doi:10.1073/pnas.93.24.13689 (1996).
- 706 35 Zhang, R. *et al.* High-Throughput Genotyping of Green Algal Mutants Reveals Random
707 Distribution of Mutagenic Insertion Sites and Endonucleolytic Cleavage of Transforming
708 DNA. *Plant Cell* **26**, 1398-1409, doi:10.1105/tpc.114.124099 (2014).

- 709 36 Zheng, S. Q. *et al.* MotionCor2: anisotropic correction of beam-induced motion for
710 improved cryo-electron microscopy. *Nat Methods* **14**, 331-332, doi:10.1038/nmeth.4193
711 (2017).
- 712 37 Rohou, A. & Grigorieff, N. CTFFIND4: Fast and accurate defocus estimation from
713 electron micrographs. *J Struct Biol* **192**, 216-221, doi:10.1016/j.jsb.2015.08.008 (2015).
- 714 38 Zivanov, J. *et al.* New tools for automated high-resolution cryo-EM structure determination
715 in RELION-3. *eLife* **7**, doi:10.7554/eLife.42166 (2018).
- 716 39 Grant, T., Rohou, A. & Grigorieff, N. cisTEM, user-friendly software for single-particle
717 image processing. *eLife* **7**, doi:10.7554/eLife.35383 (2018).
- 718 40 Punjani, A., Rubinstein, J. L., Fleet, D. J. & Brubaker, M. A. cryoSPARC: algorithms for
719 rapid unsupervised cryo-EM structure determination. *Nat Methods* **14**, 290-296,
720 doi:10.1038/nmeth.4169 (2017).
- 721 41 Punjani, A., Brubaker, M. A. & Fleet, D. J. Building Proteins in a Day: Efficient 3D
722 Molecular Structure Estimation with Electron Cryomicroscopy. *IEEE Trans Pattern Anal*
723 *Mach Intell* **39**, 706-718, doi:10.1109/TPAMI.2016.2627573 (2017).
- 724 42 Pettersen, E. F. *et al.* UCSF Chimera--a visualization system for exploratory research and
725 analysis. *J Comput Chem* **25**, 1605-1612, doi:10.1002/jcc.20084 (2004).
- 726 43 Emsley, P., Lohkamp, B., Scott, W. G. & Cowtan, K. Features and development of Coot.
727 *Acta Crystallogr D Biol Crystallogr* **66**, 486-501, doi:10.1107/S0907444910007493
728 (2010).
- 729 44 Drozdetskiy, A., Cole, C., Procter, J. & Barton, G. J. JPred4: a protein secondary structure
730 prediction server. *Nucleic Acids Res* **43**, W389-394, doi:10.1093/nar/gkv332 (2015).
- 731 45 Adams, P. D. *et al.* PHENIX: a comprehensive Python-based system for macromolecular
732 structure solution. *Acta Crystallogr D Biol Crystallogr* **66**, 213-221,
733 doi:10.1107/S0907444909052925 (2010).
- 734 46 Chen, V. B. *et al.* MolProbity: all-atom structure validation for macromolecular
735 crystallography. *Acta Crystallogr D Biol Crystallogr* **66**, 12-21,
736 doi:10.1107/S0907444909042073 (2010).
- 737 47 Sueoka, N. Mitotic replication of deoxyribonucleic acid in *Chlamydomonas reinhardi*.
738 *Proc Natl Acad Sci U S A*. **46**, 83-91, doi:10.1073/pnas.46.1.83 (1960).
- 739 48 Catanzariti, A. M., Soboleva, T. A., Jans, D. A., Board, P. G. & Baker, R. T. An efficient
740 system for high-level expression and easy purification of authentic recombinant proteins.
741 *Protein Sci* **13**, 1331-1339, doi:10.1110/ps.04618904 (2004).

- 742 49 Ewalt, K. L., Hendrick, J. P., Houry, W. A. & Hartl, F. U. In vivo observation of
743 polypeptide flux through the bacterial chaperonin system. *Cell* **90**, 491-500,
744 doi:10.1016/s0092-8674(00)80509-7 (1997).
- 745 50 Baker, R. T. *et al.* in *Ubiquitin and Protein Degradation, Part A Methods in Enzymology*
746 540-554 (2005).
- 747 51 Genkov, T., Meyer, M., Griffiths, H. & Spreitzer, R. J. Functional hybrid rubisco enzymes
748 with plant small subunits and algal large subunits: engineered rbcS cDNA for expression
749 in chlamydomonas. *J Biol Chem* **285**, 19833-19841, doi:10.1074/jbc.M110.124230 (2010).
- 750 52 Gibson, D. G. *et al.* Enzymatic assembly of DNA molecules up to several hundred
751 kilobases. *Nature methods* **6**, 343-345, doi:10.1038/nmeth.1318 (2009).
- 752 53 Li, X. *et al.* A genome-wide algal mutant library and functional screen identifies genes
753 required for eukaryotic photosynthesis. *Nat Genet* **51**, 627-635, doi:10.1038/s41588-019-
754 0370-6 (2019).
- 755 54 Martinez-Sanchez, A. *et al.* Template-free detection and classification of membrane-bound
756 complexes in cryo-electron tomograms. *Nat Methods*, doi:10.1038/s41592-019-0675-5
757 (2020).
- 758 55 Cheng, S., Cetinkaya, M. & Grater, F. How sequence determines elasticity of disordered
759 proteins. *Biophys J* **99**, 3863-3869, doi:10.1016/j.bpj.2010.10.011 (2010).
- 760

761

762 **Acknowledgements**

763 We thank Jianping Wu, Nieng Yan, Luke Mackinder, Cliff Brangwynne and members of the
764 Jonikas laboratory for helpful discussions; Ned Wingreen, Silvia Ramundo, Jessi Hennacy, Eric
765 Franklin and Alexandra Wilson for constructive feedback on the manuscript; Wolfgang
766 Baumeister and Jürgen Plitzko for providing support and cryo-ET instrumentation; and Miroslava
767 Schaffer for help with acquiring the cryo-ET data, previously published in Freeman Rosenzweig
768 *et al.*, 2017. This project was funded by National Science Foundation (IOS-1359682 and MCB-
769 1935444), National Institutes of Health (DP2-GM-119137), and Simons Foundation and Howard
770 Hughes Medical Institute (55108535) grants to M.C.J., Deutsche Forschungsgemeinschaft grant
771 (EN 1194/1-1 as part of FOR2092) to B.D.E., Ministry of Education (MOE Singapore) Tier 2 grant
772 (MOE2018-T2-2-059) to O.M.-C., UK Biotechnology and Biological Sciences Research Council
773 (BB/S015531/1) and Leverhulme Trust (RPG-2017-402) grants to A.J.M and N.A., NIH grant
774 R01GM071574 to F.M.H., Deutsche Forschungsgemeinschaft fellowship (PO2195/1-1) to S.A.P.,

775 and National Institute of General Medical Sciences of the National Institutes of Health
776 (T32GM007276) training grant to V.K.C.. The content is solely the responsibility of the authors
777 and does not necessarily represent the official view of the National Institutes of Health.

778

779 **Author contributions**

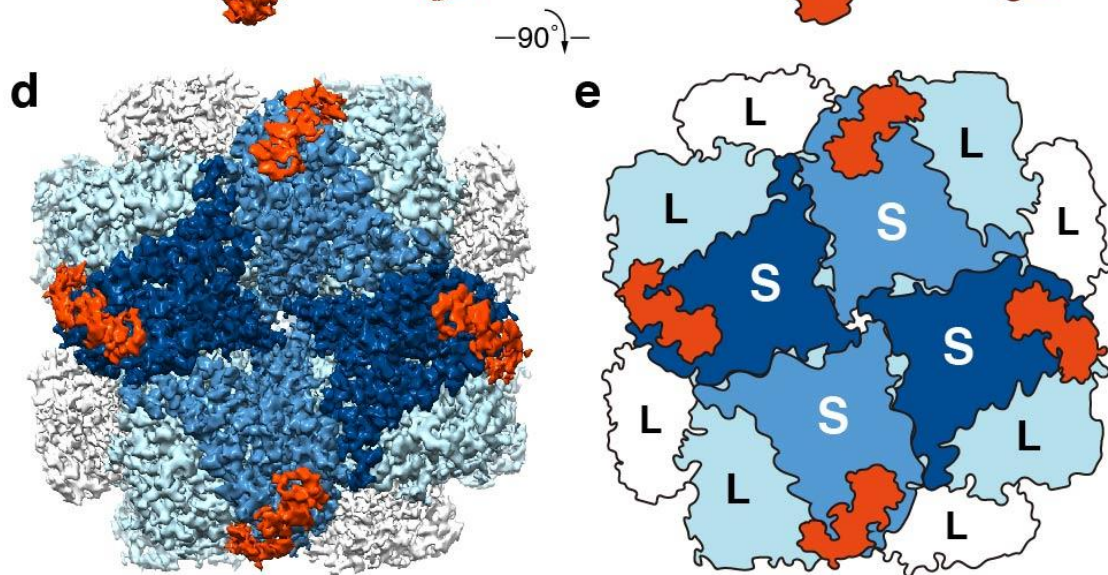
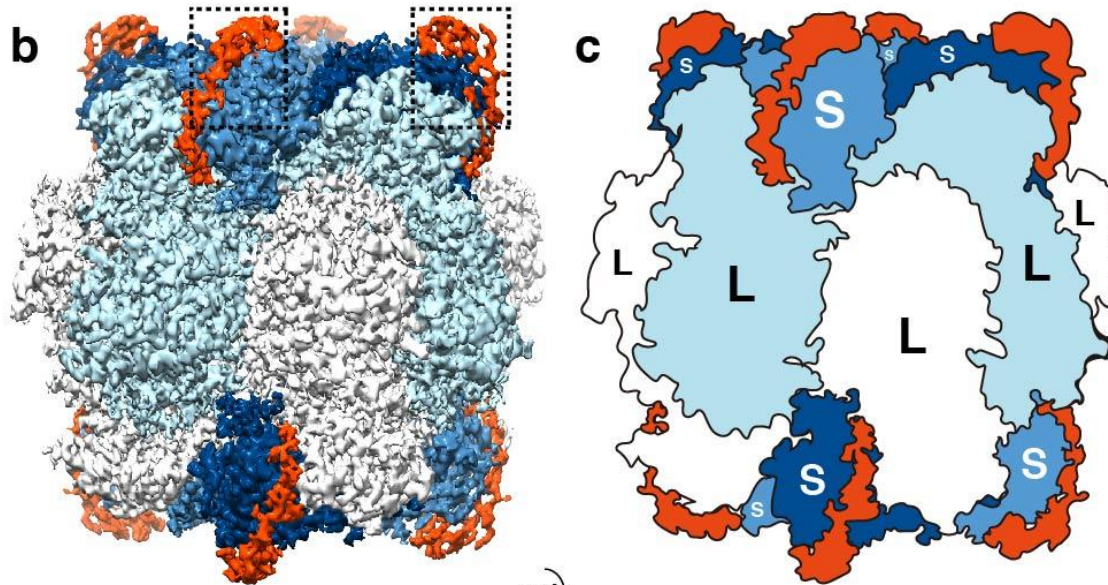
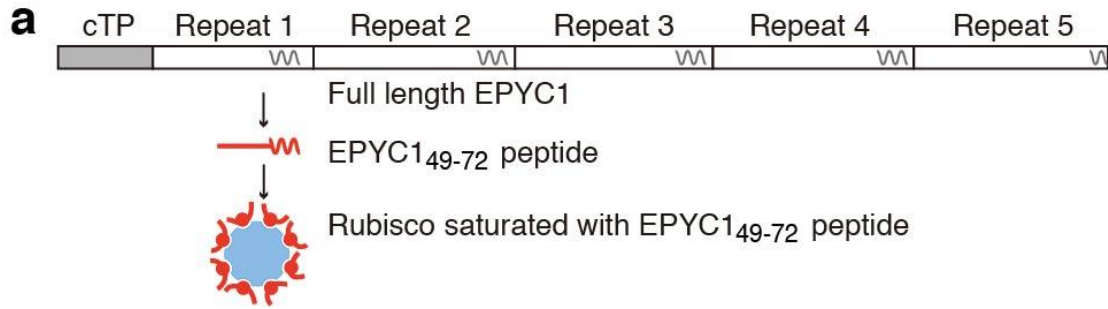
780 S.H., P.D.J., V.C., F.M.H., T.W., O.M.-C., B.D.E., and M.C.J. designed experiments. S.H.
781 identified EPYC1's Rubisco-binding regions on EPYC1 by peptide tiling array and SPR. S.H. and
782 S.A.P. prepared the Rubisco and EPYC1 peptide sample for single-particle cryo-EM; S.H., S.A.P.
783 and G.H. prepared the Rubisco samples for peptide tiling array and surface plasmon resonance.
784 H.-T.C., D.M. and Z.Y. performed Cryo-EM grid preparation, sample screening, data acquisition,
785 image processing, reconstruction and map generation. D.M. and P.D.J. carried out single-particle
786 model building and fitting and refinement. S.H., H.-T.C., D.M., P.D.J., F.M.H. and M.C.J.
787 analyzed the structures. S.H. and W.P. analyzed EPYC1 binding to Rubisco by peptide substitution
788 array and SPR. T.W. performed in vitro reconstitution phase separation experiments. N.A. and
789 A.J.M. performed yeast two-hybrid experiments. S.H. and M.T.M. made Rubisco small subunit
790 point mutants. S.H. performed spot test experiments. M.T.M. performed TEM. A.M.-S. performed
791 the cryo-ET data analysis and modeling. S.H. and M.C.J. wrote the manuscript. All authors read
792 and commented on the manuscript.

793

794 **Conflict of interest statement**

795 Princeton University and HHMI have submitted a provisional patent application on aspects of
796 the findings.

806 array of 18 amino acid peptides tiling across the full length EPYC1 sequence. **e**, Incubation of the
807 array with purified Rubisco allows identification of peptides that bind to Rubisco. **f**, Image of the
808 Rubisco binding signal from the peptide tiling array. **g**, The Rubisco binding signal was quantified
809 and plotted for each peptide as a function of the position of the middle of the peptide along the
810 EPYC1 sequence. The initial 26 amino acids of EPYC1 correspond to a chloroplast targeting
811 peptide (cTP), which is not present in the mature protein¹². Results are representative of three
812 independent experiments. **h**, The positions of EPYC1's five sequence repeats are shown to scale
813 with panel g. Predicted α -helical regions are shown as wavy lines. **i**, Primary sequence of EPYC1,
814 with the five sequence repeats aligned. In panels h and i, the regions represented by peptides
815 subsequently used for structural studies are underlined with red lines (EPYC1₄₉₋₇₂) and pink lines
816 (EPYC1₁₀₆₋₁₃₅). EPYC1₁₀₆₋₁₃₅ is an exact match to the underlined sequence of Repeats 2 and 4, and
817 has a one-amino acid difference from the corresponding region in Repeat 3 (dashed underline).

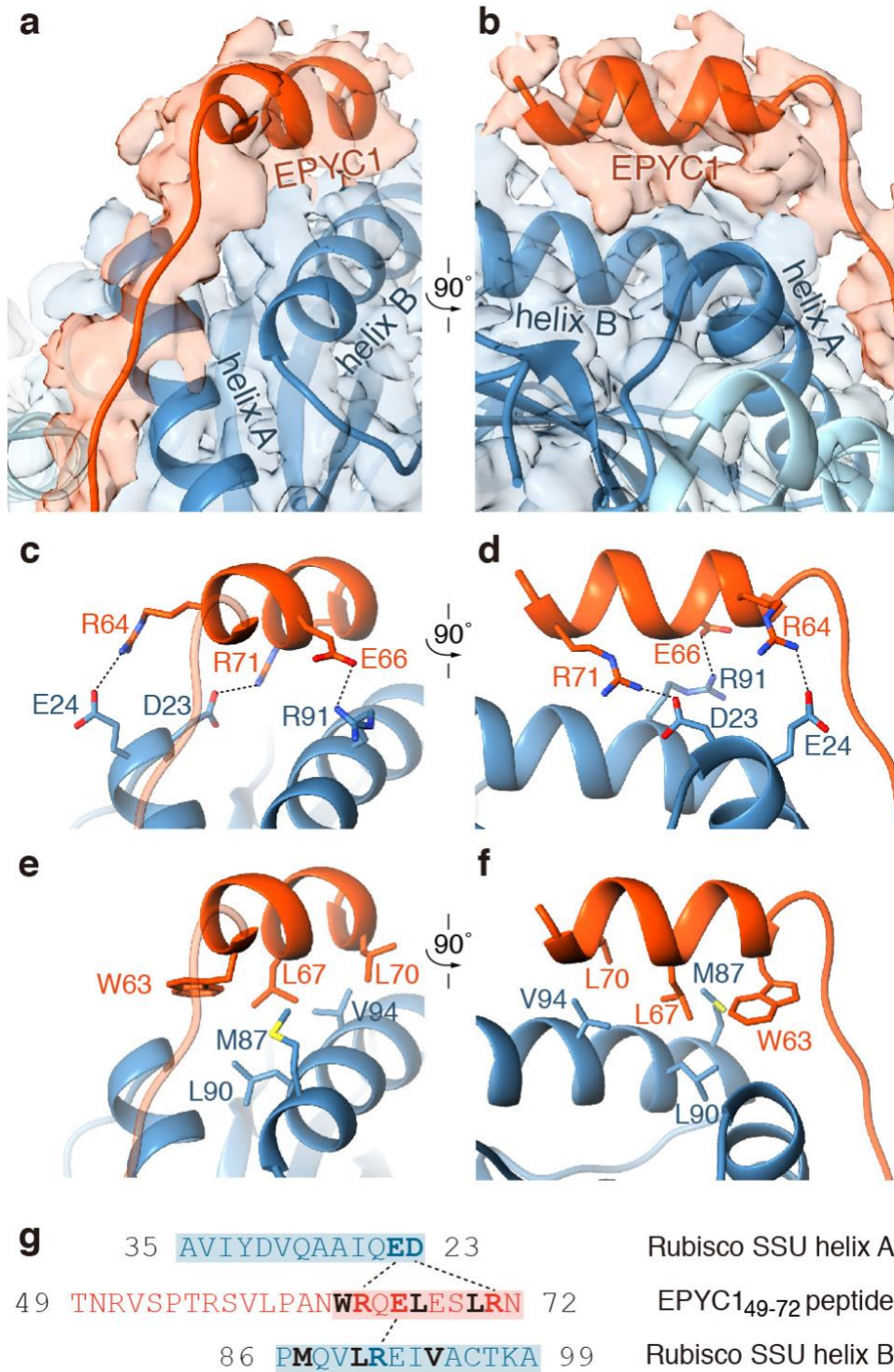


Rubisco large subunit
 Rubisco small subunit
 EPYC1 peptide

818

819

820 **Fig. 2 | EPYC1 binds to Rubisco small subunits.** **a**, Peptide EPYC1₄₉₋₇₂, corresponding to the
821 first Rubisco-binding region of EPYC1, was incubated at saturating concentrations with Rubisco
822 prior to single-particle cryo-electron microscopy. **b-e**, Density maps (b, d) and cartoons (c, e)
823 illustrate the side views (b, c) and top views (d, e) of the density map of the EPYC1 peptide-
824 Rubisco complex. Dashed boxes in panel b indicate regions shown in Fig. 3a-f.
825



826

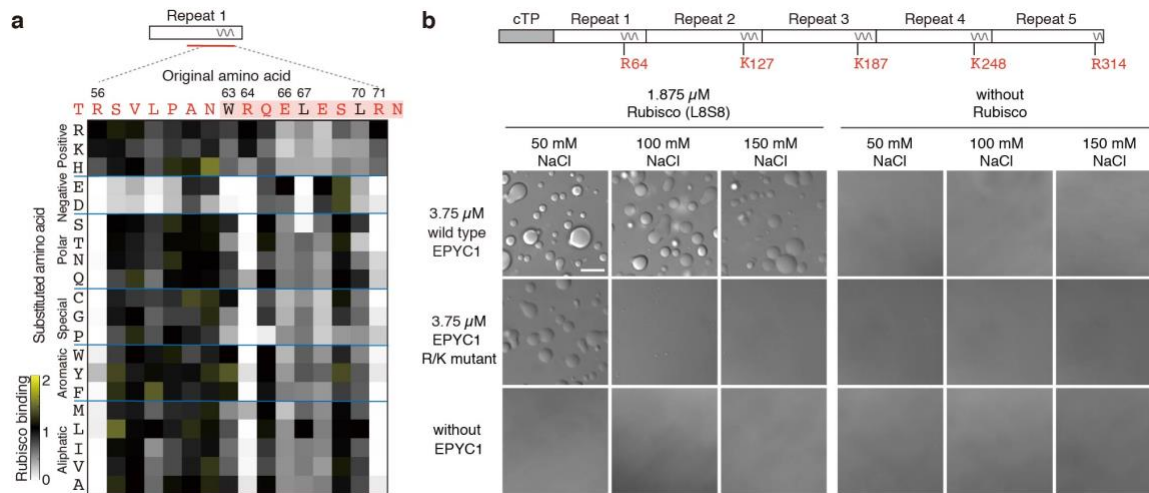
827

828 **Fig. 3 | EPYC1 binds to Rubisco small subunit α -helices via salt bridges and a hydrophobic**

829 **pocket. a-b, Front (a) and side (b) views of the EPYC1₄₉₋₇₂ peptide (red) bound to the two α -**

830 **helices of the Rubisco small subunit (blue). c-d, Three pairs of residues form salt bridges between**

831 the helix of the EPYC1₄₉₋₇₂ peptide and the helices on the Rubisco small subunit. Shown are front
832 (c) and side (d) views as in panel a and panel b. The distances from EPYC1 R64, R71 and E66 to
833 Rubisco small subunit E24, D23 and R91 are 3.06 Å, 2.78 Å, and 2.79 Å, respectively. **e-f**, A
834 hydrophobic pocket is formed by three residues of the EPYC1₄₉₋₇₂ peptide and three residues of
835 helix B of the Rubisco small subunit. Shown are front (e) and side (f) views as in panel a and panel
836 b. **g**, Summary of the interactions observed between the EPYC1₄₉₋₇₂ peptide and the two α -helices
837 of the Rubisco small subunit. Helices are highlighted; the residues mediating interactions are bold;
838 salt bridges are shown as dotted lines; residues contributing to the hydrophobic pocket are shown
839 in black.



840

841

842 **Fig. 4 | Interface residues on EPYC1 are required for binding and phase separation of**

843 **EPYC1 and Rubisco *in vitro*.** **a**, Rubisco binding to a peptide array representing every possible

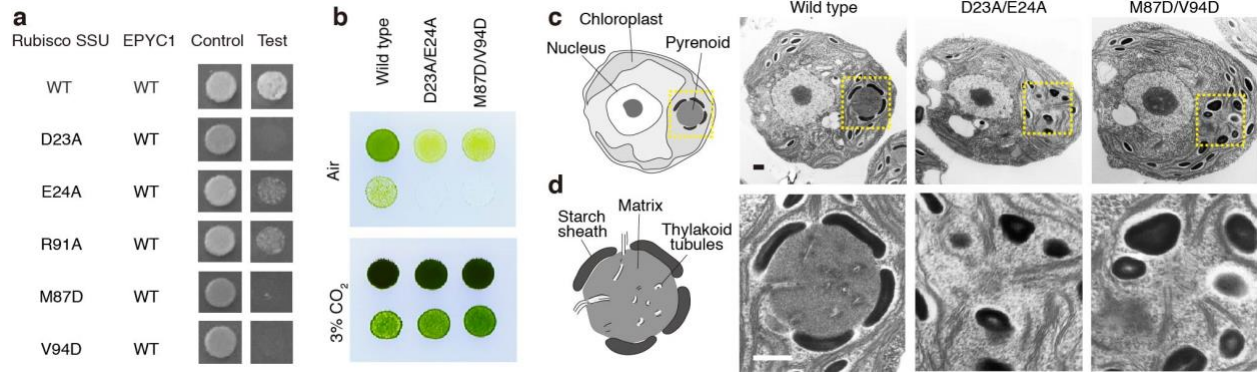
844 single amino acid substitution for amino acids 56-71 of EPYC1. The binding signal was

845 normalized by the binding signal of the original sequence. **b**, The effect of mutating the central R

846 or K in each of EPYC1's Rubisco-binding regions on *in vitro* phase separation of EPYC1 with

847 Rubisco. Scale bar = 10 μ m. For each condition, the experiment was performed twice

848 independently with similar results.



849

850

851 **Fig. 5 | Interface residues on Rubisco are required for yeast two-hybrid interactions between**

852 **EPYC1 and Rubisco, and for pyrenoid matrix formation *in vivo*.** **a**, The importance of Rubisco

853 small subunit residues for interaction with EPYC1 was tested by mutagenesis in a yeast two-hybrid

854 experiment. **b**, The Rubisco small subunit-less mutant T60 ($\Delta rbcS$) was transformed with wild-

855 type, D23A/E24A or M87D/V94D Rubisco small subunits. Serial 1:10 dilutions of cell cultures

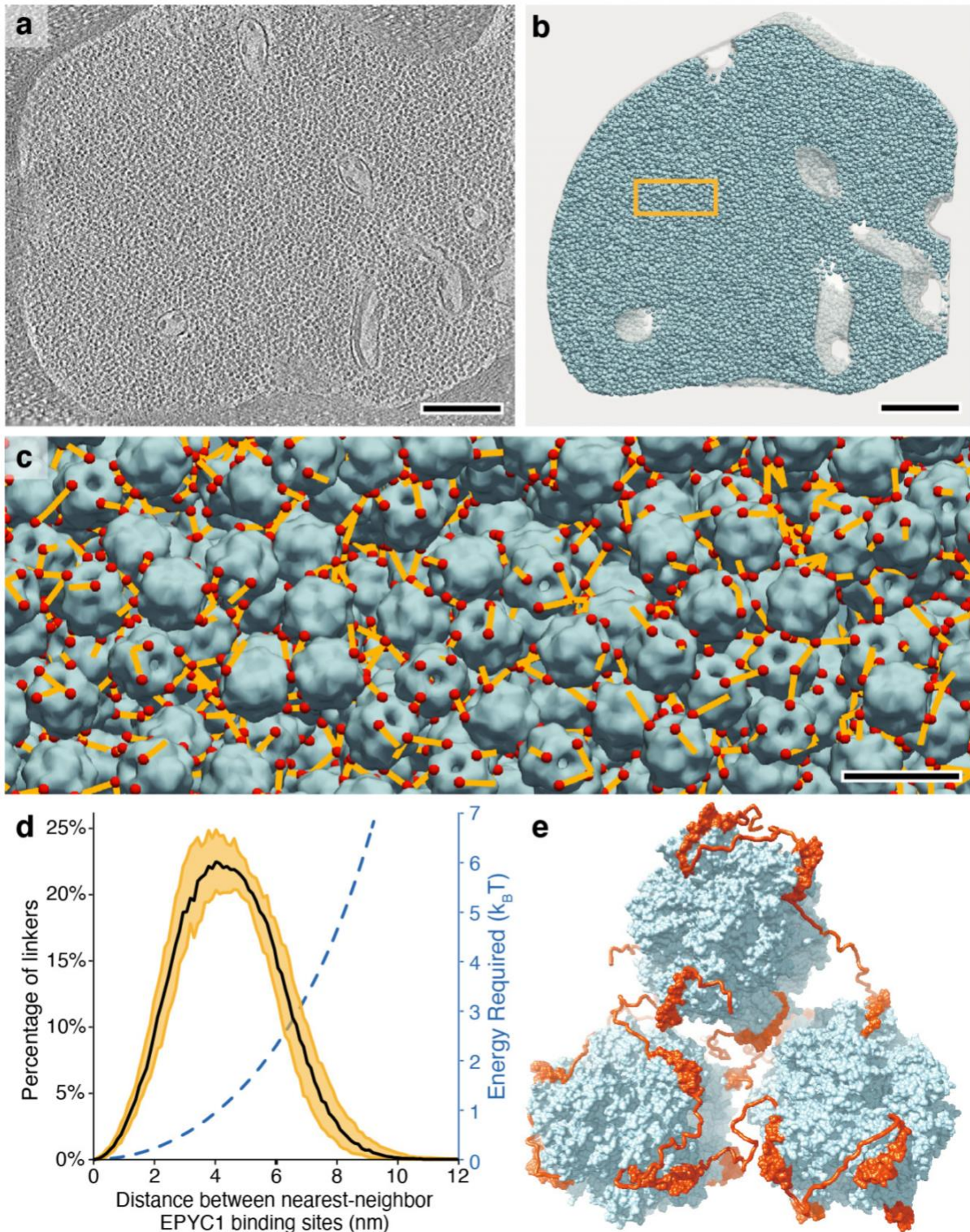
856 were spotted on TP minimal medium and grown in air or 3% CO₂. **c-d**, Representative electron

857 micrographs of whole cells (c) and corresponding pyrenoids (d) of the strains expressing wild-

858 type, D23A/E24A, and M87D/V94D Rubisco small subunit. Dashes in panel c indicate regions

859 shown in panel d. Scale bars = 500 nm. At least 25 cells were imaged for each strain; additional

860 representative images are shown in Extended Data Fig. 10c.



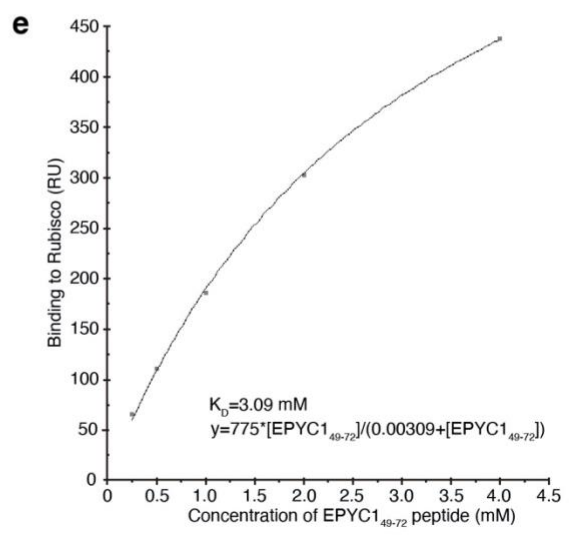
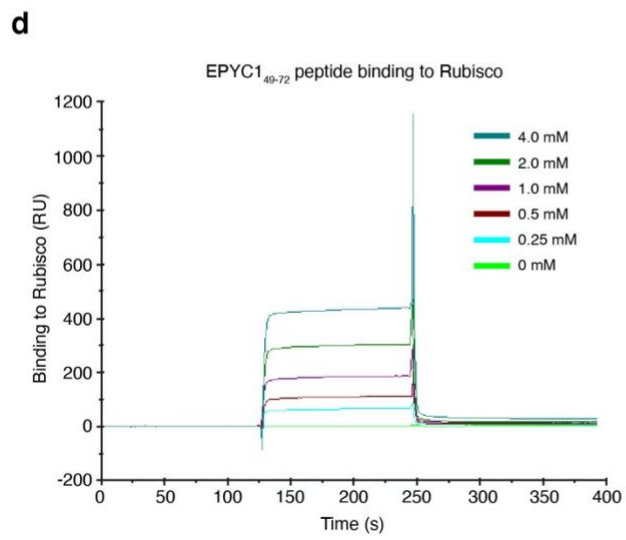
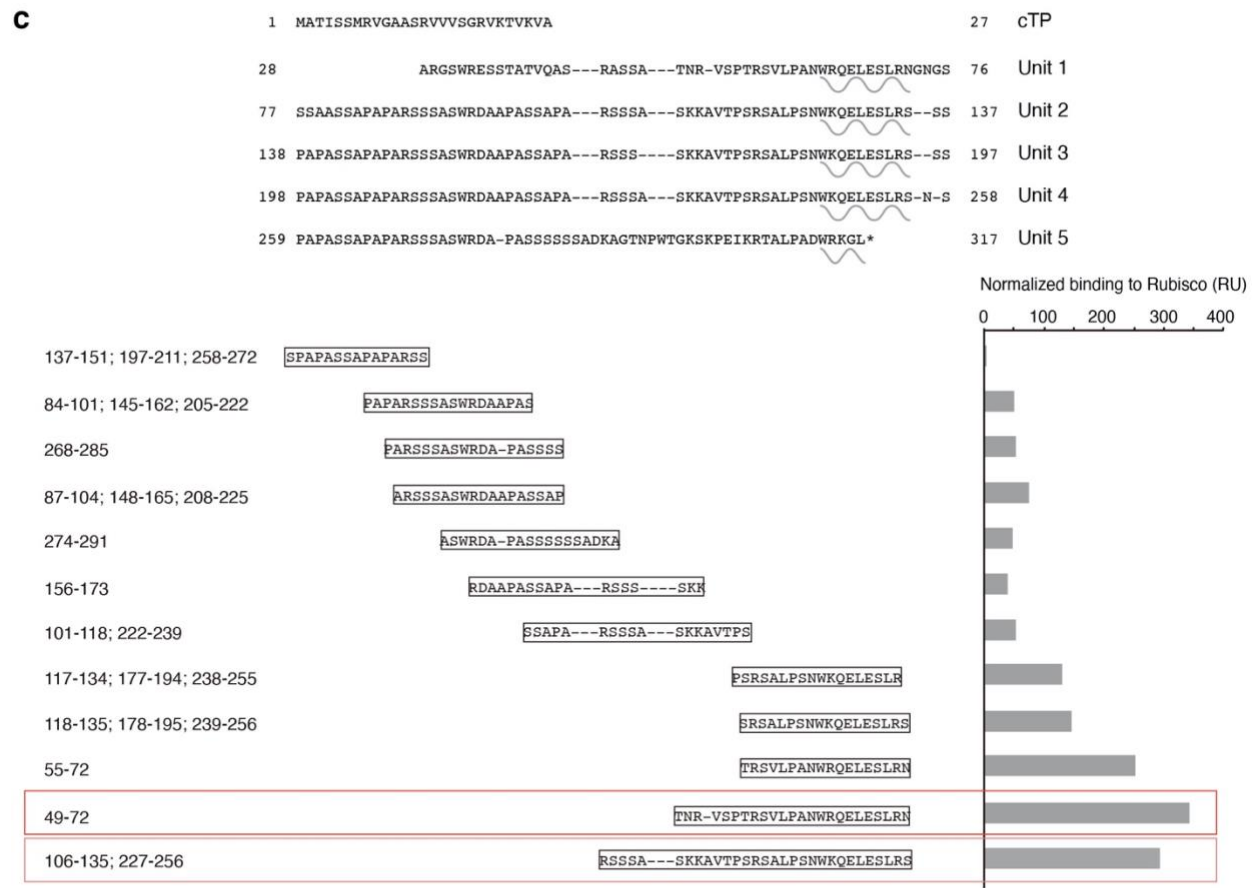
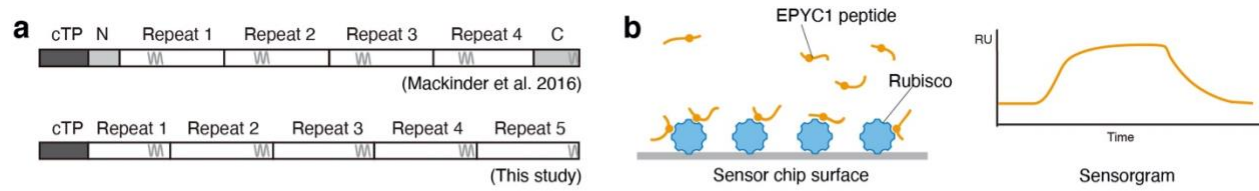
861

862

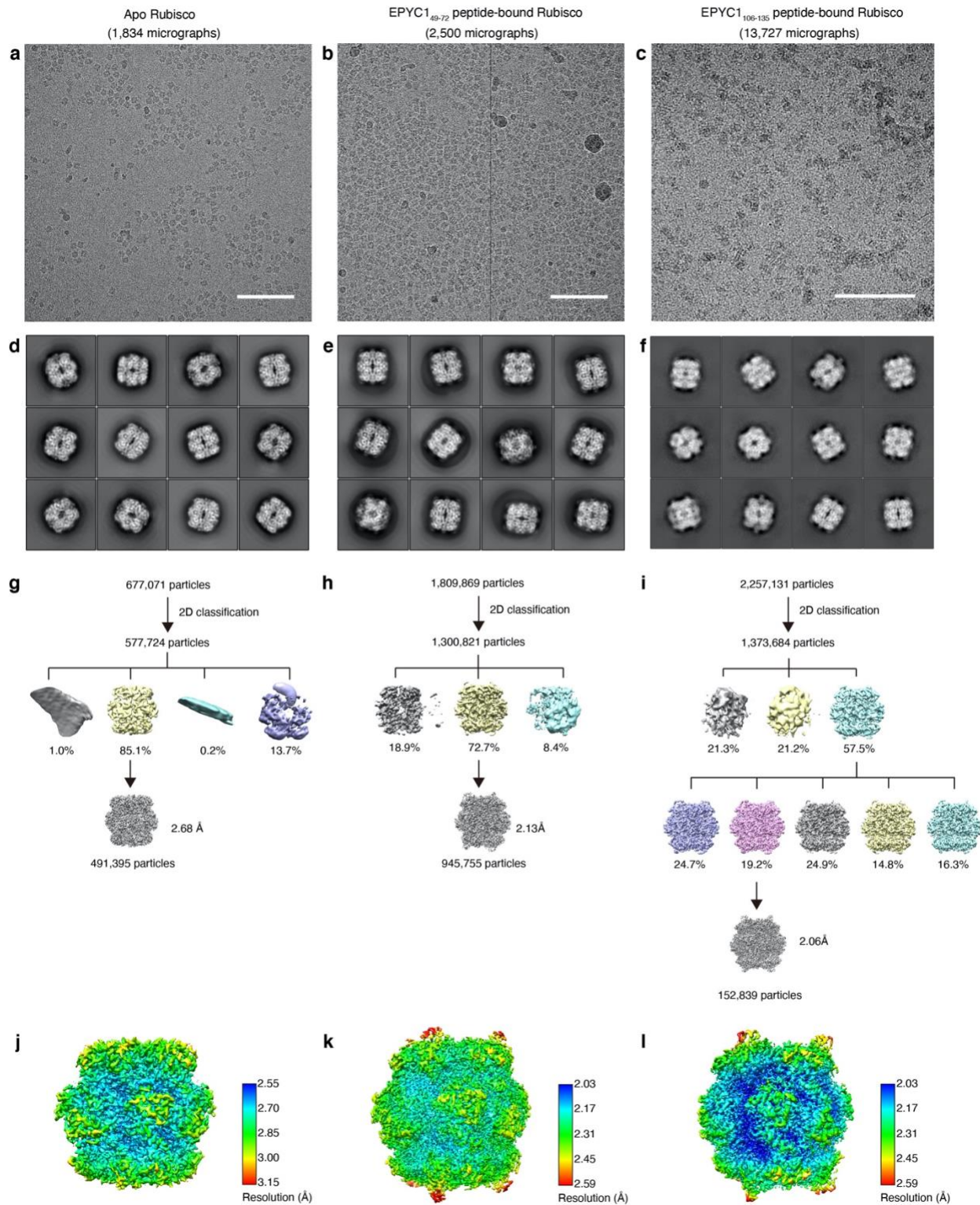
863 **Fig. 6 | A model for matrix structure consistent with *in situ* Rubisco positions and**

864 **orientations. a, The pyrenoid matrix was imaged by cryo-electron tomography⁵. An individual**

865 slice through the three-dimensional volume is shown. Scale bar = 200 nm. **b**, The positions and
866 orientations of individual Rubisco holoenzymes (blue) were determined with high sensitivity and
867 specificity (97.5% positive identification) by template matching, subtomogram averaging, and
868 classification and then mapped back into the tomogram volume shown in panel a. The yellow box
869 indicates the region shown in panel c. Scale bar = 200 nm. **c**, The distances (yellow) between the
870 nearest EPYC1-binding sites (red) on neighboring Rubisco holoenzymes (blue) were measured.
871 The view is from inside the matrix; in some cases the nearest EPYC1 binding site is on a Rubisco
872 that is out of the field of view, causing some yellow lines to appear unconnected in this image.
873 Scale bar = 20 nm. The data shown in panels a-c are representative of the five independent
874 tomograms used for this study. **d**, Histogram showing the distances between the nearest EPYC1
875 binding sites on neighboring Rubisco holoenzymes. The black line indicates the median, and the
876 yellow shading indicates 95% confidence interval based on data from five independent tomograms.
877 The estimated energy required for stretching a chain of 40 amino acids a given distance is shown
878 in blue. **e**, A 3D model illustrates how EPYC1 (red) could crosslink multiple Rubisco holoenzymes
879 (blue) to form the pyrenoid matrix. The conformations of the intrinsically disordered linkers
880 between EPYC1 binding sites were modeled hypothetically.



882 **Extended Data Fig. 1 | The EPYC1 peptides with the highest binding affinities to Rubisco**
883 **were chosen for structural studies. a,** Diagram indicating the differences between the previously
884 defined sequence repeats¹⁰ and the newly defined sequence repeats on full-length EPYC1. **b,** To
885 verify the Rubisco-binding regions on EPYC1, surface plasmon resonance (SPR) was used to
886 measure the binding of EPYC1 peptides to Rubisco. Purified Rubisco was immobilized on a sensor
887 surface, and the EPYC1 peptides in solution were injected over the surface. The binding activity
888 was recorded in real time in a sensorgram. **c,** The peptides used in SPR experiments are shown
889 aligned to the sequence as shown in Fig. 1. The Rubisco-binding signal from the SPR experiment
890 of each peptide is shown after normalization to the peptide's molecular weight. EPYC1₄₉₋₇₂ (boxed
891 in red) and EPYC1₁₀₆₋₁₃₅ (boxed in pink) were chosen for structural studies based on their
892 reproducible high Rubisco binding signal. **d,** The Rubisco-binding response of the EPYC1₄₉₋₇₂
893 peptide at different concentrations was measured by SPR. **e,** The binding responses shown in (d)
894 were fitted to estimate the K_D of EPYC1₄₉₋₇₂ peptide binding to Rubisco.



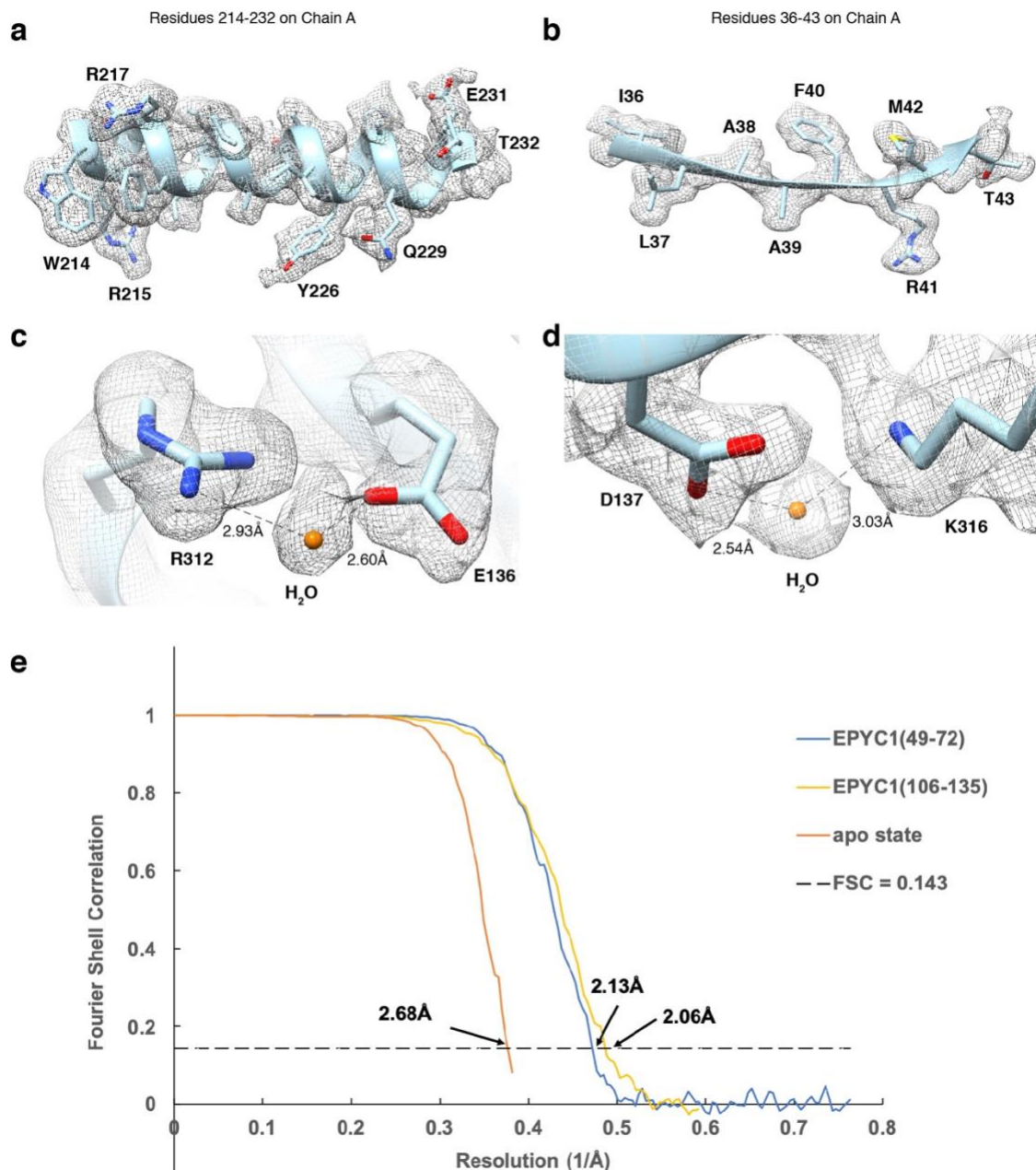
895

896

897 **Extended Data Fig. 2 | Single-particle cryo-EM data collection and image processing**

898 **procedure. a-c, Representative micrographs of the apo Rubisco sample (a), the Rubisco-EPYC1₄₉₋**

899 ₇₂ complex (b) and the Rubisco-EPYC1₁₀₆₋₁₃₅ complex (c). Scale bars = 100 nm. **d-f**,
900 Representative 2D class averages of the apo Rubisco sample (d), the Rubisco-EPYC1₄₉₋₇₂
901 complexes (e) and the Rubisco-EPYC1₁₀₆₋₁₃₅ complexes (f). **g-i**, Overview of the workflow for
902 single-particle data processing for the apo Rubisco sample (g), the Rubisco-EPYC1₄₉₋₇₂ sample (h)
903 and the Rubisco-EPYC1₁₀₆₋₁₃₅ sample (i). **j-l**, Local resolution estimation of the final refined apo
904 Rubisco map (j), the final refined Rubisco-EPYC1₄₉₋₇₂ complex map (k) and the final refined
905 Rubisco-EPYC1₁₀₆₋₁₃₅ complex map (l).

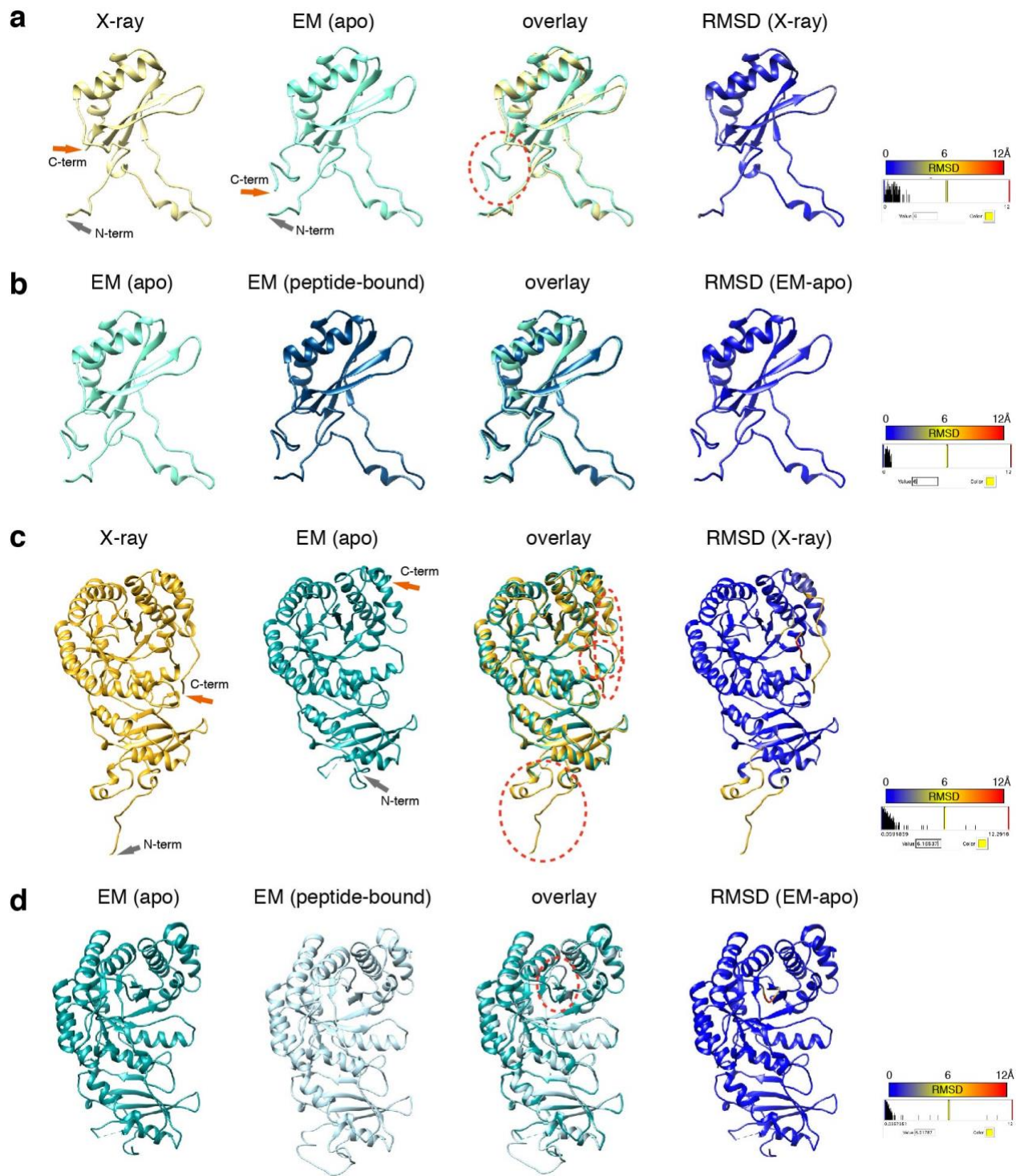


906
907

908 **Extended Data Fig. 3 | Cryo-EM analysis and resolution of apo Rubisco and Rubisco-EPYC1**
 909 **peptide complexes in this study. a-b,** Representative cryo-EM density quality showing an α -helix
 910 of residues 214-232 in chain A (one of the Rubisco large subunits) (a) and a β -sheet of residues
 911 36-43 in chain A (b) of the Rubisco-EPYC1₄₉₋₇₂ density map and structural model. The densities
 912 are shown as meshwork in gray. The backbones of the structural model are in ribbon
 913 representation, and side chains are shown in stick representation. **c-d,** Representative cryo-EM
 914 density quality showing water molecules as orange spheres. One water molecule between R312

915 and E136 on chain A is shown in panel c, and another water molecule between D137 and K316 on
916 chain A is shown in panel d. **e**, Fourier shell correlation (FSC) curves of the final density maps of
917 apo Rubisco and the Rubisco-EPYC1 peptide complexes.

918



919

920

921 **Extended Data Fig. 4 | Comparison of our EM structure of apo Rubisco and the published**
 922 **X-ray crystallography structure (1gk8) of Rubisco purified from *Chlamydomonas***
 923 ***reinhardtii*¹³, and comparison of our EM structure of apo Rubisco and Rubisco bound with**

924 **EPYC1₄₉₋₇₂ peptide.** **a**, Comparison of the structure of the small subunit of apo Rubisco obtained
925 here by EM with 1gk8. The EM structure has additional C-terminus density past residue 126,
926 circled by a red dashed line. **b**, Comparison of our two EM structures of the small subunit: from
927 apo Rubisco and from EPYC1₄₉₋₇₂ peptide-bound Rubisco. **c**, Comparison of the structure of the
928 large subunit of apo Rubisco obtained here by EM with 1gk8. The three major differences found
929 between the X-ray structure and the EM structure of the large subunit are circled with red dashed
930 lines. **d**, Comparison of our two EM structures of the large subunit: from apo Rubisco and from
931 EPYC1₄₉₋₇₂ peptide-bound Rubisco. The major difference found between the EPYC1₄₉₋₇₂ peptide-
932 bound structure and the apo EM structure was the loop between K175 and L180 of the large
933 subunit, which is shown circled by a red dashed line.



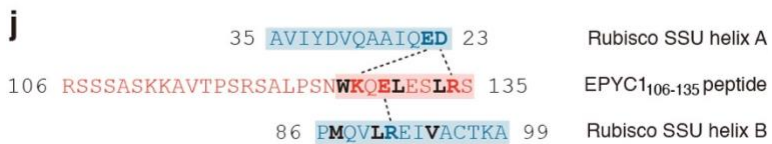
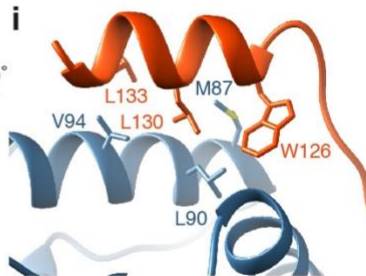
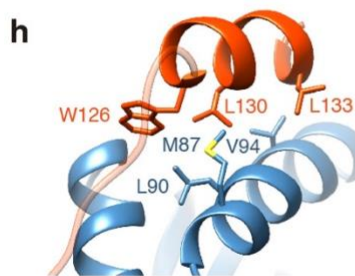
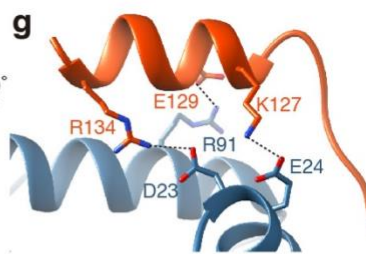
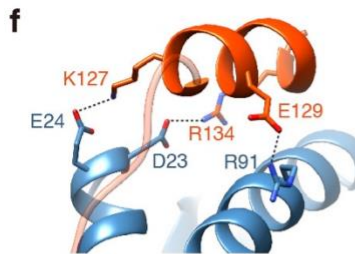
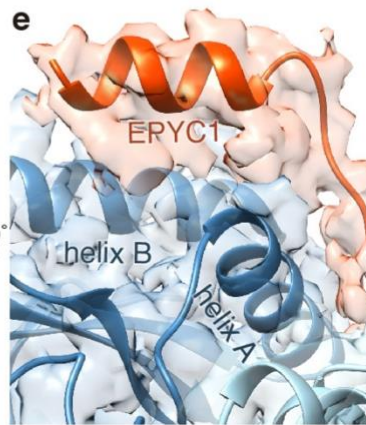
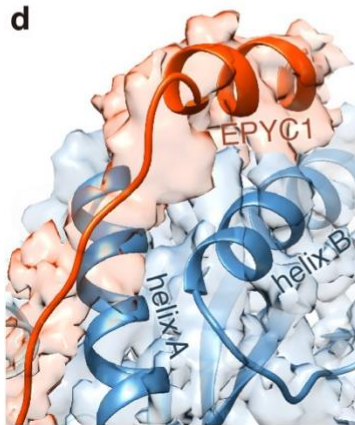
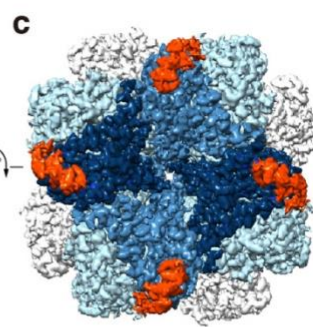
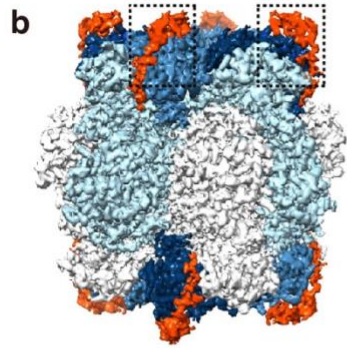
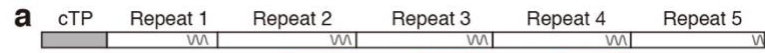
934

935 **Extended Data Fig. 5 | Additional residues may contribute to the interaction between EPYC1**
936 **and Rubisco.** Our Rubisco-EPYC₁₄₉₋₇₂ peptide structure suggests that R56 of the EPYC₁₄₉₋₇₂
937 peptide may interact with D31 of the Rubisco small subunit and E433 of the Rubisco large subunit
938 (the atoms of the backbone of E433 are also shown to display the possible interaction). R51 of the
939 EPYC₁₄₉₋₇₂ peptide may form a salt bridge with Y32 of the Rubisco small subunit. Residues S57

940 and V58 of the EPYC₁₄₉₋₇₂ peptide are close to D31 in the structure, which may explain why
941 replacing either of these residues with a negatively charged residue disrupts binding (Fig. 4a).

942

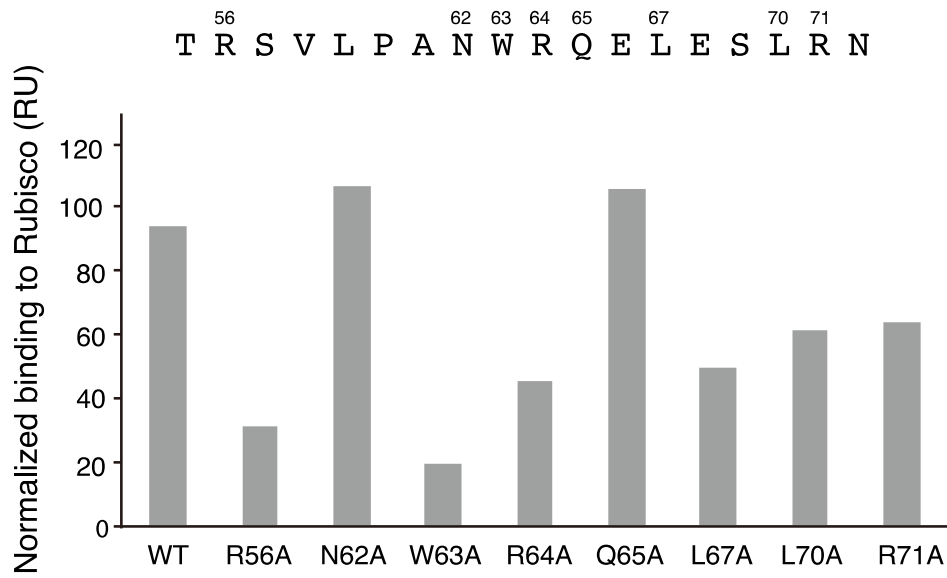
943



944

945

946 **Extended Data Fig. 6 | The EPYC1₁₀₆₋₁₃₅ peptide binds to Rubisco small subunit α -helices via**
947 **salt bridges and a hydrophobic pocket in a similar manner to the EPYC1₄₉₋₇₂ peptide. a,** The
948 EPYC1₁₀₆₋₁₃₅ peptide represents the second, third and fourth Rubisco-binding regions of EPYC1
949 indicated by pink lines and dash line (the peptide is a perfect match to the second and fourth
950 Rubisco-binding regions, and there is a one-amino acid difference between the peptide and the
951 third repeat). **b-c,** Side view (b) and top view (c) of the density map of the EPYC1₁₀₆₋₁₃₅ peptide-
952 Rubisco complex. Dashes in panel b indicate regions shown in panels d-i. **d-e,** Front (d) and side
953 (e) views of the EPYC1₁₀₆₋₁₃₅ peptide (red) bound to the two α -helices of the Rubisco small subunit
954 (blue). **f-g,** Three pairs of residues form salt bridges between the helix of the EPYC1₁₀₆₋₁₃₅ peptide
955 and the helices on the Rubisco small subunit. Shown are front (f) and side (g) views as in panel d
956 and panel e. The distances from EPYC1 K127, R134 and E129 to Rubisco small subunit E24, D23
957 and R91 are 2.96 Å, 3.17 Å, and 2.68 Å, respectively. **h-i,** A hydrophobic pocket is formed by
958 three residues of the EPYC1₁₀₆₋₁₃₅ peptide and three residues of helix B of the Rubisco small
959 subunit. Shown are front (h) and side (i) views as in panel d and panel e. **j,** Summary of the
960 interactions observed between the EPYC1₁₀₆₋₁₃₅ peptide and the two α -helices of the Rubisco small
961 subunit. Helices are highlighted; the residues mediating interactions are bold; salt bridges are
962 shown as dotted lines; residues contributing to the hydrophobic pocket are shown in black. **k,** Color
963 keys used in this figure.
964
965



966

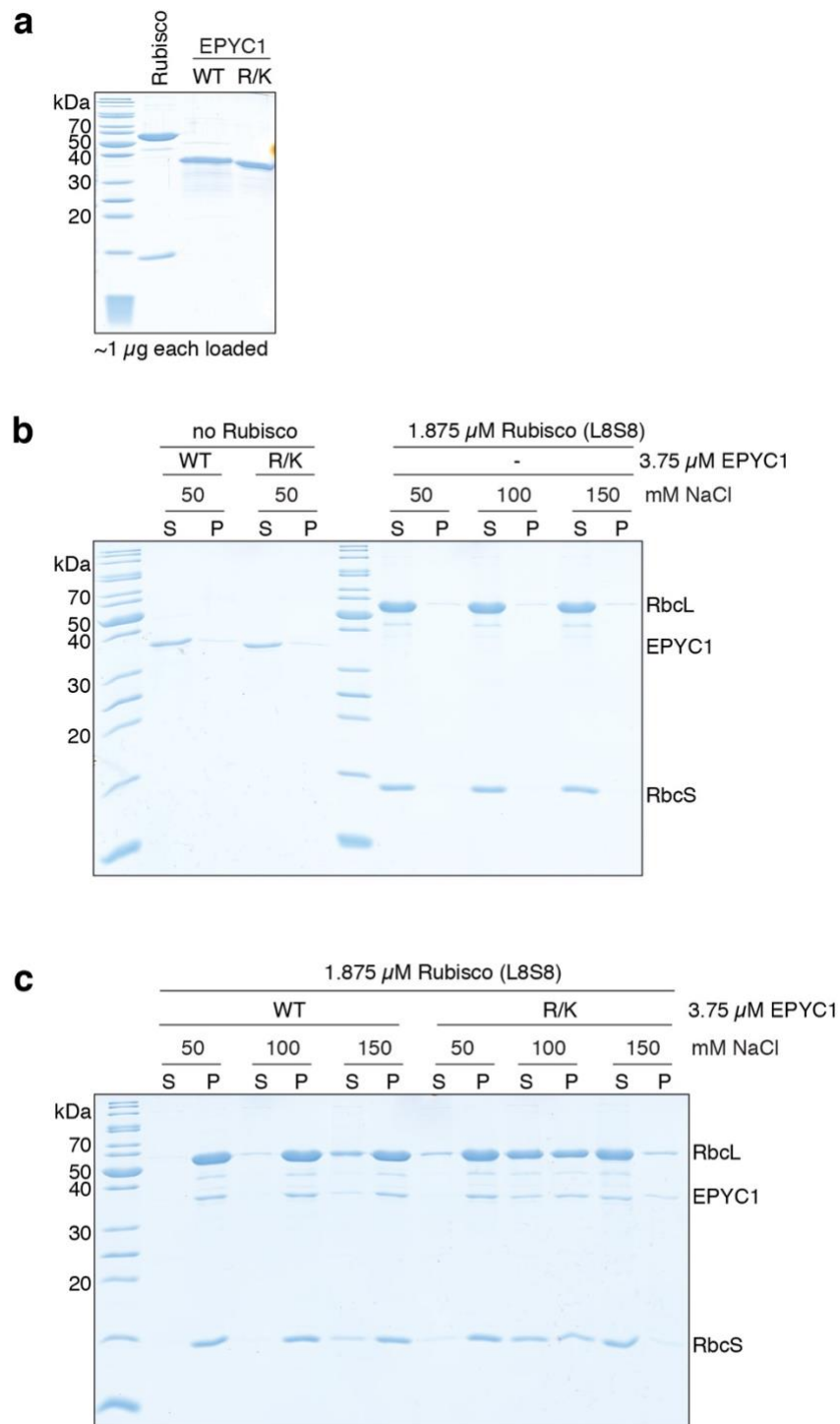
967

968 **Extended Data Fig. 7 | Surface plasmon resonance analysis of binding of point mutants of**

969 **EPYC1⁵⁵⁻⁷² to Rubisco.** The wild-type (WT) peptide or peptides with the indicated mutations

970 were synthesized, and their Rubisco-binding signal was measured by surface plasmon resonance.

971



972

973

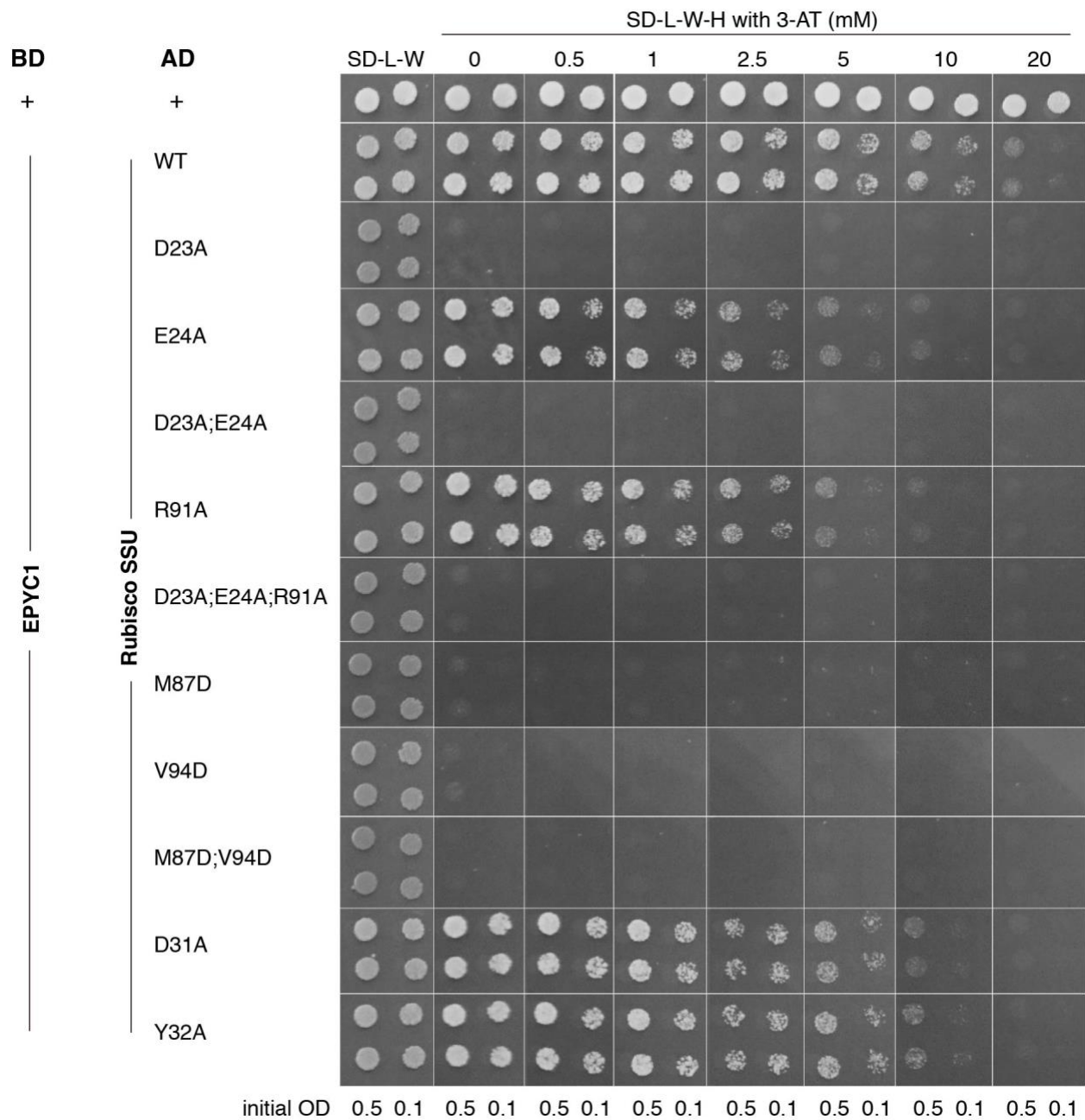
974 **Extended Data Fig. 8 | Interface residues on EPYC1 identified by cryo-EM are important**

975 **for binding and phase separation of EPYC1 and Rubisco.** **a**, SDS-PAGE analysis of purified

976 proteins used for *in vitro* phase separation experiments. WT = wild-type EPYC1; R/K =

977 EPYC1^{R64A/K127A/K187A/K248A/R314}. **b-c**, A droplet sedimentation assay was used as a readout of phase

978 separation complementary to the microscopy analyses shown in Fig. 4b. Proteins at indicated
979 concentrations were mixed and incubated for 10 minutes, then condensates were pelleted by
980 centrifugation. Supernatant (S) and pellet (P) fractions were run on a denaturing gel. The negative
981 controls with no Rubisco or with no EPYC1 are shown in (b), and the wild-type Rubisco with
982 wild-type EPYC1 or mutant EPYC1 are shown in (c). Data shown here are representative of two
983 independent replicates.



984

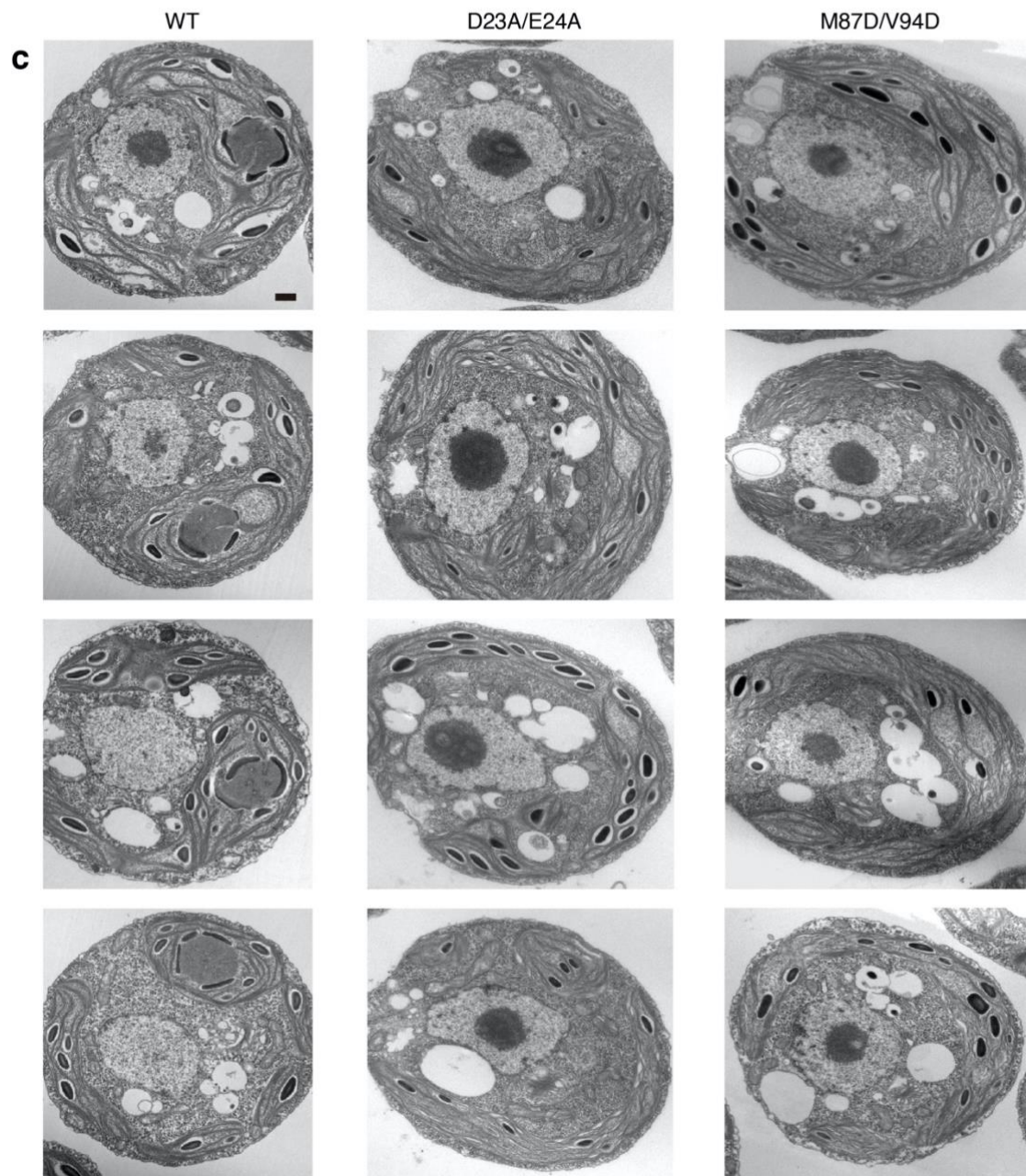
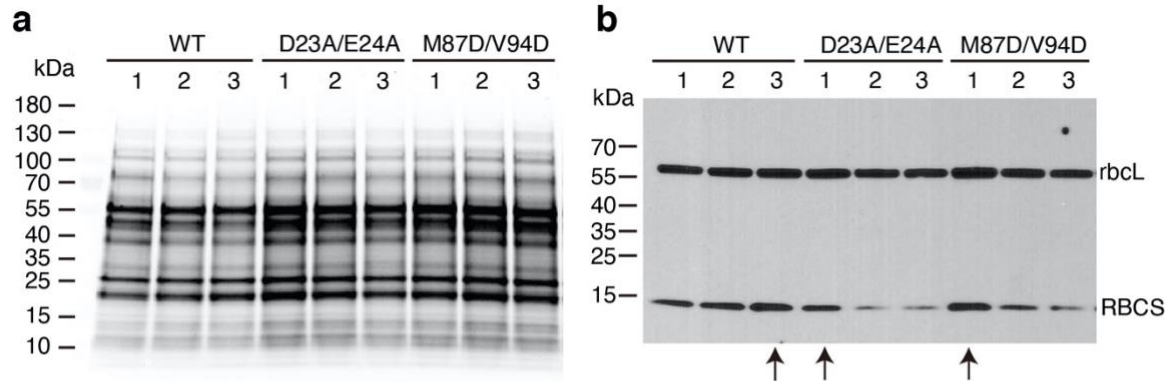
985

986 **Extended Data Fig. 9 | Yeast two-hybrid assays of interactions between EPYC1 and wild-**

987 **type or mutated Rubisco small subunit.** Colonies are shown after 3 days growth on plates. A

988 subset of the data shown in this figure is shown in Fig. 5a.

989



991 **Extended Data Fig. 10 | Selection of the Rubisco small subunit mutant strains for phenotype**
992 **analysis. a,** The Rubisco small subunit-less mutant T60 (*Arbcs*) was transformed with DNA
993 encoding wild-type and mutant Rubisco small subunits (RBCS) to produce candidate
994 transformants with the genotypes *Arbcs;RBCS^{WT}*, *Arbcs;RBCS^{D23A/E24A}*, and *Arbcs;RBCS^{M87D/V94D}*.
995 Total protein extracts for three strains from each transformation were separated on a
996 polyacrylamide gel. **b,** The gel shown in panel a was probed by Western blot using a polyclonal
997 antibody mixture that detects both large and small Rubisco subunits. The experiments shown in
998 panel a and b were performed once for selecting the candidate transformants with the highest
999 RBCS expression level from each genotype, in case any phenotype may be caused by low
1000 expression level of Rubisco. Selected strains are indicated by an arrow below the lanes and were
1001 used for the subsequent phenotypic analyses shown in Fig. 5 and panel c. **c,** Additional
1002 representative TEM images of whole cells of the strains expressing wild-type, D23A/E24A, and
1003 M87D/V94D Rubisco small subunit. Scale bar = 500 nm. For each strain, at least 25 images (one
1004 image for one cell) were taken and showing similar results.

1005 **Extended Data Table 1 | Cryo-EM data collection and refinement.**

1006

	#1 Apo Rubisco (EMDB-22401) (PDB 7JN4) (EMPIAR-10503)	#2 EPYC1 ₄₉₋₇₂ peptide- bound Rubisco (EMDB-22308) (PDB 7JFO) (EMPIAR-10502)	#3 EPYC1 ₁₀₆₋₁₃₅ peptide- bound Rubisco (EMDB-22462) (PDB 7JSX) (EMPIAR-10501)
Voltage (kV)	300	300	300
Camera/detector	K2	K2	K3
Magnification	22,500	22,500	81,000
Pixel size (Å)	1.31	0.655	0.844
Defocus range (μm)	-1.5 to -3.0	-1.5 to -3.0	-1 to -1.6
Exposure time (s)	10	10	3.56
No. movie frames	50	50	60
Electron dose (e ⁻ /Å ²)	58	58	60
No. micrographs	1,834	2,500	13,727
No. initial particles	677,071	1,809,869	2,257,131
No. final particle	491,395	945,755	152,839
Symmetry	D4	D4	D4
Resolution (Å)	2.68	2.13	2.06
Map sharpening <i>B</i> factor (Å ²)	-100.04	-77.55	-47.75

1007

1008

1009

1010 **Extended Data Table 2 | The amino acid residues that form the Rubisco-binding regions on**
 1011 **EPYC1 homologs and the residues that form the EPYC1 binding site on the surface of**
 1012 **Rubisco, appear to be conserved across the order Volvocales.** Residues with roles in the
 1013 binding interface are bolded. Residues that are different from the *Chlamydomonas reinhardtii*
 1014 sequence are highlighted in grey.
 1015

Species	First Rubisco-binding region on EPYC1 homolog	Rubisco SSU helix A	Rubisco SSU helix B
<i>Chlamydomonas reinhardtii</i>	TRSVLPAN WRQELESLRN	DE QIAAQVDYIVA	PMQV L REIVACTKA
<i>Tetrabaena socialis</i>	TRSVLPAN WRQELESLRG	DE QIAAQVDYIVA	PMQV L REIV S CT R A
<i>Gonium pectorale</i>	TRSVLPAN WRQELESLRN	DE QIAAQVDYIVA	PMQV L REIVACTKA
<i>Volvox carteri</i>	TRSVLPAN WRQELESLRN	DE QIAAQVDYIVA	PMQV L REIVACTKA

1016